Coastal Engineering 166 (2021) 103867

Contents lists available at ScienceDirect

Coastal Engineering

journal homepage: http://www.elsevier.com/locate/coastaleng

Experimental study of debris transport driven by a tsunami-like wave: Application for non-uniform density groups and obstacles

Hyoungsu Park [a,*], Myung-Jin Koh [a], Daniel T. Cox [b], Mohammad Shafiqual Alam [b], Sungwon Shin [c]

[a] Department of Civil and Environmental Engineering, University of Hawai'i at Manoa, Honolulu, HI, 96822, United States
[b] School of Civil and Construction Engineering, Oregon State University, Corvallis, OR, 97331, United States
[c] Department of Marine Science and Convergence Engineering Hanyang University, Ansan, Kyunggi-do, Republic of Korea

ARTICLE INFO

Keywords:
Debris transport
Density
Dislocation
Obstacle
Tsunami

ABSTRACT

Water-borne disaster debris can exacerbate the damage on the built-environment through debris impact and debris damming loads and by decreasing the functionality of infrastructure systems after these events. Therefore, an understanding of disaster debris transport is essential for disaster management. In this paper, an experimental study of tsunami-driven debris spreading over a flat testbed was conducted considering different density conditions of debris elements. Debris elements of two different materials (densities) were considered various debris groups and starting orientation. The final dislocations and local velocity of debris elements were measured optically and compared to flow velocity. Among two debris elements in a debris group, it was found that debris elements of higher density affected the mean longitudinal displacement of the less dense debris, but the less dense debris did not affect the displacement of higher density debris. Also, it was found that the initial orientations of the debris groups had no measurable impact on the final displacement. The effects of obstacles on the passage of debris and the probability of collision to obstacles were examined and the process of debris-debris and debris-obstacle interactions from debris entrainment to final dislocation was studied. It was found that the less dense debris had a higher probability of collision with the obstacles compared to the more dense debris case. However, when the debris types were mixed, the less dense debris had a lower probability of collision. Finally, the characteristics of debris dislocation and velocity fields under various density conditions as a group were also evaluated. The reflected wave and interaction among different debris play a role in the probability of collision. However, the density of each debris element was a dominant factor in determining the collision probability.

1. Introduction

Extreme coastal events like hurricanes and tsunamis often generate and transport debris resulting in severe damage to civil infrastructure systems (e.g., Chock et al., 2013; Naito et al., 2014) and often adversely affecting the resilience and recovery process of communities (Çelik et al., 2015). In particular, water-borne debris such as shipping containers, vehicles, and wood logs are well known to exacerbate the structural damage on the built environment through the debris impact (collision) and damming loads (e.g., Riggs et al., 2014; Yeh et al., 2014). Moreover, debris transported over the land often decreases the functionality of critical facilities and block access for initial rescue and recovery. It is also reported that the hurricane-driven coastal debris removal could account for approximately 27% of the total disaster recovery cost in the USA (FEMA, 2007). Therefore, a better understanding of water-driven debris transport is essential to predict damages and losses on coastal communities and to develop a mitigation plan to minimize those losses and improve the resilience against future extreme coastal events.

Over the years, our understanding of tsunami disaster debris has enriched from field reconnaissance, numerical simulations, and laboratory experiments. Several field surveys reported marine debris transport in the open ocean originating from tsunami runup and drawdown on land which is relevant for pollution (e.g., Martinez et al., 2009; Praesetya et a., 2012; Murray et al., 2018) and changes in marine ecology (e.g, Miller et al., 2018) as well as marine debris transport close to shore in navigable waterways and overland. A few debris studies debris carried overland such as large boulders and sediment deposits to

* Corresponding author.
E-mail address: Hpark9@hawaii.edu (H. Park).

https://doi.org/10.1016/j.coastaleng.2021.103867
Received 5 September 2020; Received in revised form 3 February 2021; Accepted 13 February 2021
Available online 19 February 2021

determine, for example, the intensity of past tsunami events (e.g., Bourgeois and Maclnnes, 2010; Paris et al., 2010, Etienne et al., 2011). For the built environment, there are relatively few documented studies of debris transport overland. Naito et al. (2014) performed the first field survey to evaluate the overall transport of debris from the 2011 Tohoku Tsunami. They tracked the final dislocation of large debris such as shipping containers and vessels, then estimated the angle of debris distribution from the origin, which is the spreading angle with a limit distance (areas) based on the quantity at the origin. This approach is adopted in the current ASCE7/SEI 7–16 in Chapter 6 (ASCE, 2017) to evaluate the debris hazard region under potential tsunami debris impact loading if the region has relevant sources of debris such as vessel, shipping container, logs, and boulder.

There have been several numerical investigations for the aforementioned observed tsunami debris phenomena, particularly boulder transport (e.g., Imamura et al., 2008) and sediment transport (Sugawara et al., 2014) to aid in the understanding of tsunami hazards. However, there are relatively fewer studies of tsunami debris transport in the engineering context, for example, the transport of construction debris from damaged buildings and other components of the built environment. In their review of tsunami debris transport and loads, Nistor et al. (2017a) cites several numerical studies but had focused primarily on modeling a single or relatively few debris elements leading to impact on structures. More recently, Park and Cox (2019) showed how a Lagrangian tracking method with ad-hoc assumptions for the initiation and grounding of debris can be used to advect debris at a community-wide scale. Kihara and Kaida (2020) used a debris tracking model to assess the probability of debris striking an object. They compared their work to laboratory simulations and considered two important aspects: the effects of reflected waves from structures on the debris as it approaches the structure, and the diffusion of debris as it is transported. For the latter, they added a numerical diffusion to recreate the conditions observed in the laboratory.

Subsequent to the 2011 Tohoku tsunami, there have been a number of tsunami debris studies based on scaled hydraulic experiments (e.g., Riggs et al., 2014; Aghl et al., 2015; Xia et al., 2014; Ko et al., 2015; Stolle et al., 2017; Stolle et al., 2018a; Shekhar et al., 2020). Most of these studies have mainly focused on debris-structures impact or damming loads using varied shapes (e.g., shipping container, vehicles, box, and pole) and materials (e.g., Wood, and Polyethylene). However, there have been relatively fewer experimental studies that focused on tsunami driven debris motions and transportation including debris entrainment and spreading. Yao et al. (2014) conducted a study of debris transport over a sloped bed with tsunami-like flow conditions, evaluating the final dislocation of debris and compared that to the maximum flow inundation. Rueben et al. (2015) examined the effect of multiple debris and fixed obstacles on debris motion, tracking both individual debris elements as well as the center of mass of the group. Shafiei et al. (2016) developed an equation for the debris speed under dam-break flow conditions as a function of the leading-edge velocity of flow, mass, and projected area of single debris using an implemented accelerometer in debris. Goseberg et al. (2016) reported a significant effect of the presence of obstacles on the moving distance of debris utilizing Bluetooth Low Energy wireless connection to track the debris motion. Nistor et al. (2017b) conducted a physical modeling study and determined the debris spreading angle, suggesting that the spreading angle increases with the number of debris likely due to the debris interaction. Stolle et al. (2018b) and Stolle et al. (2020) used a statistical approach considering debris speed and motions combined with non-dimensional parameters to predict the probability of debris transport, analogous to approaches in wind engineering (Tachikawa, 1983; Lin and Vanmarcke, 2008). The dependency of initial positions of two debris including gap-ratio and lateral displacement is measured focusing on debris' rotation as well as longitudinal and lateral displacement (von Hafen et al., 2021). Table 1 summarizes detailed information of recent tsunami-driven debris transport experiments. However, most of the tsunami-driven debris transport studies to date relied on relatively a small number of debris and debris configurations and they were still limited to in representing the complicated multi-debris transport process including its generation, entrainment, interactions with obstacles, spreading, and grounding.

In this study, we performed an experimental study of multi-debris transport using grouped debris, which comprises of two types of debris with different density. We utilized optical measurement and observed the details on the debris entrainment, debris floating, and dragging under the various initial debris setups under a tsunami-like wave condition. The major objectives of this study include: 1) A better understanding of the overall process of multi-debris transport and its characteristics. 2) Evaluating the effects of varied density of grouped multi-debris in the debris transport. 3) Evaluating the effects of downstream obstacles to debris transport. These objectives are achieved in the following sections. Section 2 introduces the experiment setup and Section 3 provides the optical measurement process and preliminary results. Section 4 shows the results of debris advection including final debris moving distance, spreading angle, probability of collision to obstacles, and debris flow fields under varied grouped debris conditions. Section 5 discusses the limitations of current work, and Section 6 summarized the general findings in this study and suggested possible future works.

Table 1
The summary of experimental research on tsunami-driven debris transportation.

	Tracking Method	Debris				Interaction w/Obstacles	Wave Type
		Shape	Dimension (cm) H × W × L	Number	Material (Specific Gravity)		
Yao et al. (2014)	Optical	Square Box	0.5 × 0.5 × 1.0	10, 20, 30	Polyethylene SG = 0.92	No	Solitary wave
Rueben et al. (2015)	Optical	Square Box	40 × 60 × 60	1, 4, 9	Plywood SG = 0.71	Yes	Tsunami like wave
Shafiei et al. (2016)	Optical, Sensor	Disc	(D)20 × 5	1	Acrylic + add mass SG = 0.32, 0.46, 0.58	Yes	Dam break wave
Goseberg (2016)	[a]Smart debris	Shipping Container	6 × 6 × 15	3, 6	Polyethylene (w/sensor) SG = 0.92	Yes	Tsunami like wave
Nistor et al. (2017)	[a]Smartdebris, Optical	Shipping Container	6 × 6 × 15	1, 3, 9, 18	Polyethylene(w/sensor) SG = 0.92	No	Tsunami like wave
Stolle et al. (2020);	Optical	Shipping Container	6 × 6 × 15	1, 3, 6, 2, 6, 12	Polyethylene SG = 0.418	Yes	Dam break wave
Current study	Optical	Square Box	5 × 10 × 10	20	Wood (SG = 0.65), HDPE (SG = 0.99)	Yes	Tsunami like wave

[a] Smart debris indicates the debris utilized the wireless sensor inside of debris for tracking. (Goseberg et al., 2016).

2. Experimental setup

The physical experiments were performed in the Directional Wave Basin at Oregon State University (Fig. 1). The wave basin was 48.8 m long (x-direction), 26.5 m wide (y-direction), and 2.1 m deep (z-direction), and was equipped with a segmented piston-type wavemaker with a maximum full stroke of 2.1 m and maximum velocity of 2.0 m/s. For the debris experiment, the uniform sloped and elevated bathymetry, installed in the middle of the basin (Fig. 1) were utilized. The profile of bathymetry consisted of an 11.29 m flat section starting from the wavemaker ($x = 0$ m), 1:20 slope extended from $x = 11.29$ m to $x = 31.29$ m, and a 10 m flat section, elevated 1.0 m above the basin floor and extending to $x = 41.29$ m. The total width of the slope and the elevated area was 10 m ($y = -5$ m–5 m), and two brick walls (top and bottom) were installed as sidewalls at the sloped and flat sections. The bathymetry was capped with smooth concrete. Two multi-grouped debris sources (red and yellow checkerboard in Fig. 1a) were located at the start of the flat section ($x = 31.29$ m). Sidewalls ran parallel to the x-axis on either side, and the end of the flat section was open to the surrounding water such that the inundating water could flow unimpeded over the back of the test section. This is the same general set-up used for other overland flow experiments (e.g., Tomizek et al., 2020, Duncan et al., submitted).

The instrumentation consisted of nine surface piercing wire resistance wave gages (wg1 – wg9), eight ultrasonic wave gages (USWG1 – USWG8), and seven acoustic-Doppler velocimeters (ADV1 – ADV7). Seven of the USWGs and all of the ADVs were installed on the movable bridge, originally located over the slope (indicated by a dotted rectangle with sensor locations in Fig. 1a). USWG8 was installed at the end of the flat section. The movable bridge was fixed during the debris transport test and it was shifted 7.23 m forward (x-direction) to measure the kinematics conditions (surface elevation and velocity) at the flat section without debris cases (indicated by the second dotted rectangle in Fig. 1a). The shifted location for seven USWGs and ADVs, which were installed on the movable bridge, are marked as $USWG_h$ and ADV_h in Fig. 1a. Table 2 summarizes the coordinates of the instrumentation. Note that the wavemaker displacement (wmdisp) was also recorded for all tests and is not used for this paper but is available for future numerical modeling efforts. Also, note that ultrasonic wave gages locations are reported for the two cases, for the debris transport tests and the kinematics tests in parenthesis.

Fig. 2 shows three photographs of the testbed and instrumentation. Fig. 2a shows a general view of the testbed without debris and the movable bridge on the flat section and Fig. 2b shows an example of a debris test setup using two groups of debris and eight obstacles (white boxes). Fig. 2a and b shows the two sidewalls in the flat section as well as the end of the test section that allowed the overland flow to spill into the basin. The orange grid lines in Fig. 2a and b were painted with 2 m spacing to provide a frame of reference for the video cameras. Fig. 2c shows the mounting device for four video cameras. These cameras were mounted on a steel frame and elevated at the center of the flat section to record the debris transport for all trials. The cameras are referred to as CAM1, CAM2, CAM3, and CAM4 (Fig. 1a) and had an overlapping field of view of a diagonal quarter of the flat region. The framerate of each camera was set at 29.97 Hz, and each camera had a resolution of 1 080 by 1920 pixels. The facility lighting was controlled to provide optical contrast between the debris and to minimize the reflection from the water.

The debris was constructed from two types of material, high-density polyethylene (HDPE, painted orange) and Douglas-fir (wood, painted yellow) to study the different densities on debris transport (Fig. 3). The debris pieces measured 10.2 cm (L) by 10.2 cm (W) and 5.1 cm (H). About a 10 cm debris length scale was chosen based on an approximate geometric scale of 1:50 for this experiment. At this scale, the modeled

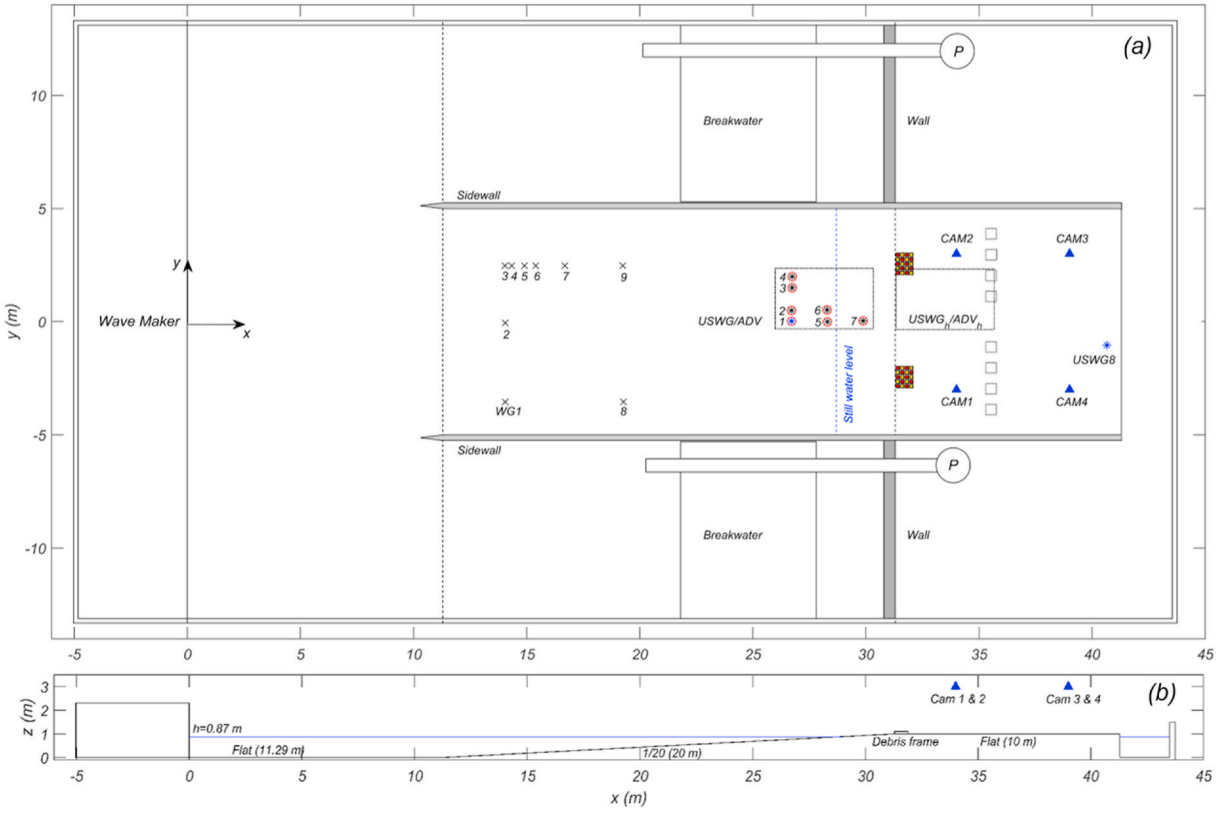

Fig. 1. Sketch of the experimental setup: (a) plan and (b) profile view. At Fig. 1a, each symbol of ' × ' and '*' indicates the wire resistance wave gage (WG) and ultrasonic wave gage (USWG), while '○' indicates the location of acoustic-Doppler Velocimeter (ADV), which are overlapped to USWG locations. Triangle indicates the location of four cameras. In Fig. 1b, the debris frame indicates the location of the initial debris setup for our experiment, and more details are available in Fig. 5.

Table 2
Instrument locations.

Instrument description	Instrument	x (m)	y (m)	z (m)
Wavemaker displacement	wmdisp	-	0.00	-
Resistive wave gage	WG1	14.052	−3.540	-
Resistive wave gage	WG2	14.048	−0.056	-
Resistive wave gage	WG3	14.039	2.473	-
Resistive wave gage	WG4	14.341	2.482	-
Resistive wave gage	WG5	14.899	2.477	-
Resistive wave gage	WG6	15.394	2.474	-
Resistive wave gage	WG7	16.688	2.470	-
Resistive wave gage	WG8	19.278	−3.538	-
Resistive wave gage	WG9	19.246	2.494	-
Ultrasonic wave gage	USWG1	26.708	0.024	2.294
	($USWG_h1$)	(33.941)	(0.024)	(2.294)
Ultrasonic wave gage	USWG2	26.701	0.498	2.302
	($USWG_h2$)	(33.931)	(0.498)	(2.302)
Ultrasonic wave gage	USWG3	26.750	1.502	2.309
	($USWG_h3$)	(33.973)	(1.502)	(2.309)
Ultrasonic wave gage	USWG4	26.757	1.992	2.305
	($USWG_h4$)	(33.976)	(1.992)	(2.305)
Ultrasonic wave gage	USWG5	28.298	−0.003	2.357
	($USWG_h5$)	(35.531)	(−0.003)	(2.357)
Ultrasonic wave gage	USWG6	28.286	0.523	2.428
	($USWG_h6$)	(35.516)	(0.523)	(2.428)
Ultrasonic wave gage	USWG7	29.878	0.037	2.376
	($USWG_h7$)	(37.111)	(0.037)	(2.376)
Ultrasonic wave gage	USWG8	40.655	−1.039 (−1.039)	1.769
Acoustic-Doppler Velocimeter	ADV1	26.715	−0.019	1.020
	(ADV_h1)	(33.949)	(−0.019)	(1.020)
Acoustic-Doppler Velocimeter	ADV2	26.705	0.479	1.049
	(ADV_h2)	(33.935)	(0.479)	(1.049)
Acoustic-Doppler Velocimeter	ADV3	26.736	1.494	1.053
	(ADV_h3)	(33.959)	(1.494)	(1.053)
Acoustic-Doppler Velocimeter	ADV4	26.735	1.992	1.041
	(ADV_h4)	(33.954)	(1.992)	(1.041)
Acoustic-Doppler Velocimeter	ADV5	28.296	−0.026	1.018
	(ADV_h5)	(35.530)	(−0.026)	(1.018)
Acoustic-Doppler Velocimeter	ADV6	28.290	0.473	1.011
	(ADV_h6)	(35.520)	(0.473)	(1.011)
Acoustic-Doppler Velocimeter	ADV7	29.867	−0.018	1.018
	(ADV_h7)	(37.101)	(−0.018)	(1.018)

debris would correspond to a prototype size of approximately 5 m which would be larger than a passenger vehicle and smaller than a shipping container. These are the two classes of debris considered, for example, in the engineering design of structures to withstand tsunami loads (e.g., Chock et al., 2016).

Although geometric similitude has been used to describe the size of the debris, we did not attempt to scale the density or proper center of gravity of the debris for debris such as shipping containers or vehicles. As noted by one of the reviewers, the detailed motion of the debris under real-world conditions for these debris types would require careful consideration of the correct specific gravity and center of gravity.

During preliminary tests, we observed that the motion of the debris was sensitive to the friction between the bottom of the debris and the concrete floor of the test section. Further, we observed that the wood debris would become worn during these tests, unlike the HDPE which became scratched initially and then remained fairly consistent without additional wear. To keep the surface roughness the same between the two debris types and to prevent changes in the surface of the wood debris during multiple trials, we removed a 2 mm layer from the bottom of the wood debris and replaced it with the same thickness of HDPE. Both the HDPE and wood debris were roughened on the concrete surface to create a consistent physical roughness for all debris elements before starting the final experiments presented here.

The measured mean density of HDPE and wood debris was 987 (11.7) kg/m^3 and 648 (17.6) kg/m^3, respectively, after painting. The standard deviation is presented in parenthesis. The weight of each HDPE and wood debris was 0.524 kg and 0.326 kg, and the draft of each HDPE and Wood debris was 5.03 cm and 3.30 cm, respectfully. The wood debris was wiped dry at the end of each day and reweighed to determine whether the density changed during the testing. We observed less than 2% change in density of the wood debris throughout the testing which lasted several days. We maintained the same initial conditions on the test section by manually removing water on the test surface using floor squeegees after each trial, and then it took an additional 10 min to set up the next tests. Therefore, the concrete itself was wet before each trial as can be seen in Fig. 2b, but there were no areas with measurable standing water before testing.

The static friction coefficient (μ_s) was measured for both debris types under the slightly wet conditions of the test section using $F = \mu_s N$ where F is the horizontal force and N is the normal force. We connected a small load cell to individual pieces of debris and then applied a horizontal force until the debris started to move. These tests were conducted at 16 locations within the 10 m by 10 m test section and were repeated 3 times at each location for a total of 48 tests for each debris type. The averaged static friction coefficient and standard deviations under the test conditions were $\mu_s = 0.66$ (0.07) for HDPE and $\mu_s = 1.28$ (0.13) for wood, with the standard deviation in parenthesis. The measured friction coefficient is an important parameter of future numerical modeling of debris transportation, as the friction coefficient will be decisive in comparing experimental and numerical results. It is noted that the coefficient of friction for the wood debris is nearly double that of the HDPE debris, even though the wood debris has the same HDPE material on the bottom. This difference is likely due to surface tension effects between the debris and the concrete which was not considered when estimating the friction coefficient.

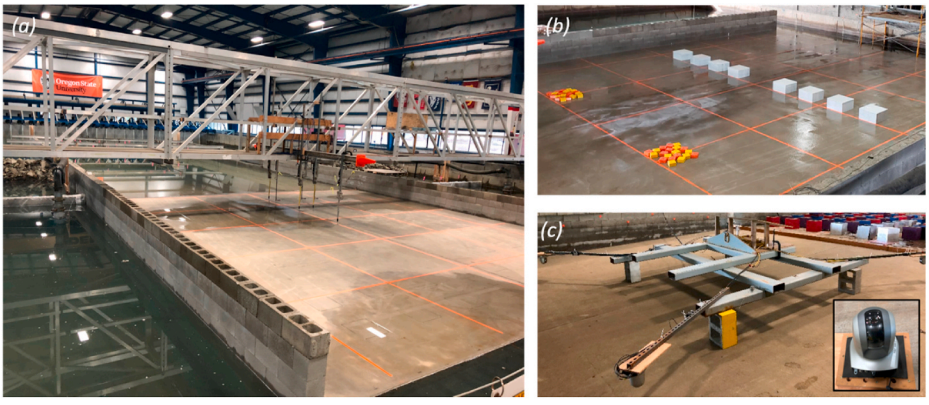

Fig. 2. Photographs of the debris test setup. (a) Overview of testbed without debris, (b) Overview of the testbed in other direction with two setups of debris and eight obstacles, (c) Steel frame for the camera mounting and snapshot of the camera (inner photo).

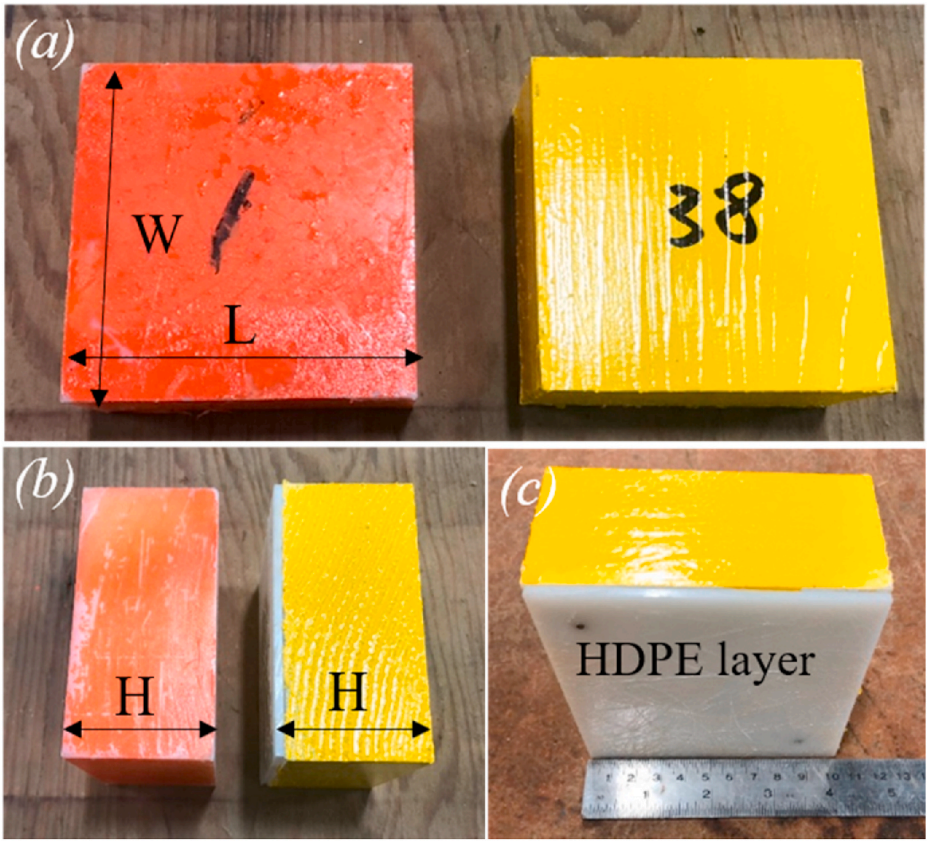

Fig. 3. (a) Plan view of HDPE (orange) and Wood debris (yellow), (b) Side views (c) HDPE layer (2.5 mm) for Wood debris. Both HDPE and wood debris have the same size. (For interpretation of the references to color in this figure legend, the reader is referred to the Web version of this article.)

3. Experimental procedure

3.1. Water depth and wave conditions

To reduce the overall complexity of the experiments, we performed all tests using the same water level and wave condition (wavemaker displacement time series). To arrive at an appropriate depth and wave condition, we tested several waves and water depth conditions to meet four criteria. First, we wanted a relatively long inundation period and flow conditions with a Froud number of Fr ~1.0 based on numerical simulations of tsunami inundation flow (e.g., Park et al., 2018). Second, we wanted to avoid a breaking wave directly on or in front of the debris because the splash up and generation of air bubbles could interfere with the optical measurement. Moreover, this type of entrainment mechanism may be less common based on the video of debris transported during the 2011 Tohoku tsunami. Third, we wanted the debris to come to rest within the 10 m test section without having the debris wash over the end ($x = 42\ m$). Fourth, for simplicity, we wanted to avoid reflected waves that could have been large enough to cause subsequent motion to the debris.

After trial and error, we arrived at a condition with a fixed water depth ($z = 0.78\ m$) and the wavemaker displacement time series as shown in Fig. 4a (solid black line) based on previous experiments in this facility for tsunami inundation (e.g., Park et al., 2013) and debris impact (e.g., Ko et al., 2015). Fig. 4a also shows the fluctuation of surface elevation (η) at the wavemaker (*wmwg*, dashed blue). The wavemaker displacement time series was determined using an error function rather than solitary wave theory so that we could maximize the full, 2 m stroke of the wavemaker. Then, the time of the wavemaker displacement was adjusted to achieve the conditions described earlier. The second peak at t ~37 *s* is the wave reflected from the test section reaching the wavemaker. Active absorption was not used, so the reflected wave was re-reflected from the wavemaker and inundated the test section a second time. However, the amplitude of this second inundation was much smaller than the first and did not Tcause any further displacement of debris.

Fig. 4b, c, and d show how the free surface profile varies as the initial wave propagates over the slope (4b and 4c) and at the flat region (4d). The maximum measured amplitude occurred at USWG *5* ($h_{max} = 0.14\ m$) before the water shoreline at $x = 31.29\ m$. The period of the positive amplitude surface elevation was 11.1 *s* at wg1 and increase to 13.2 *s* at USWG *5*. As the wave inundated over the testbed, the maximum amplitude decreased, and inundation duration increased as can be seen in Fig. 4d. Considering the draft of each HDPE (5.03 cm) and wood (3.30 cm) debris, the entrained HDPE debris will start grounding before reach to the $USWG_h$ 1 (x = 33.941 *m*), while wood debris will start grounding around at $USWG_h$ 5 (x = 35.531 *m*).

The corresponding velocity of the wave in the *x*-direction from ADV shows that the measured peak velocity was about 1.0 m/s at $USWG_h1$ and ranged from 0.55 to 0.65 m/s at $USWG_h5$, and $USWG_h7$. (Fig. 4e). The estimated Froude number at the peak amplitude from USWG $_h1$ to $USWG_h$ 7 ranged from $Fr = 1.11$ to $Fr = 0.71$. It is noted that ADV sensors could not capture leading-edge flow successfully (e.g., Park et al., 2013), and data are discontinued because of relatively low surface elevation. Later, we use the optical measurements to infer the velocity of the leading edge.

We acknowledge that the overall inundation duration time is too short compared to a tsunami at the prototype scale. So, these tests represent only an idealized model of tsunami inundation. Future experiments should consider tsunami inundation with longer durations.

3.2. The initial position of grouped debris and test case

The processes of the initial debris entrainment and subsequent

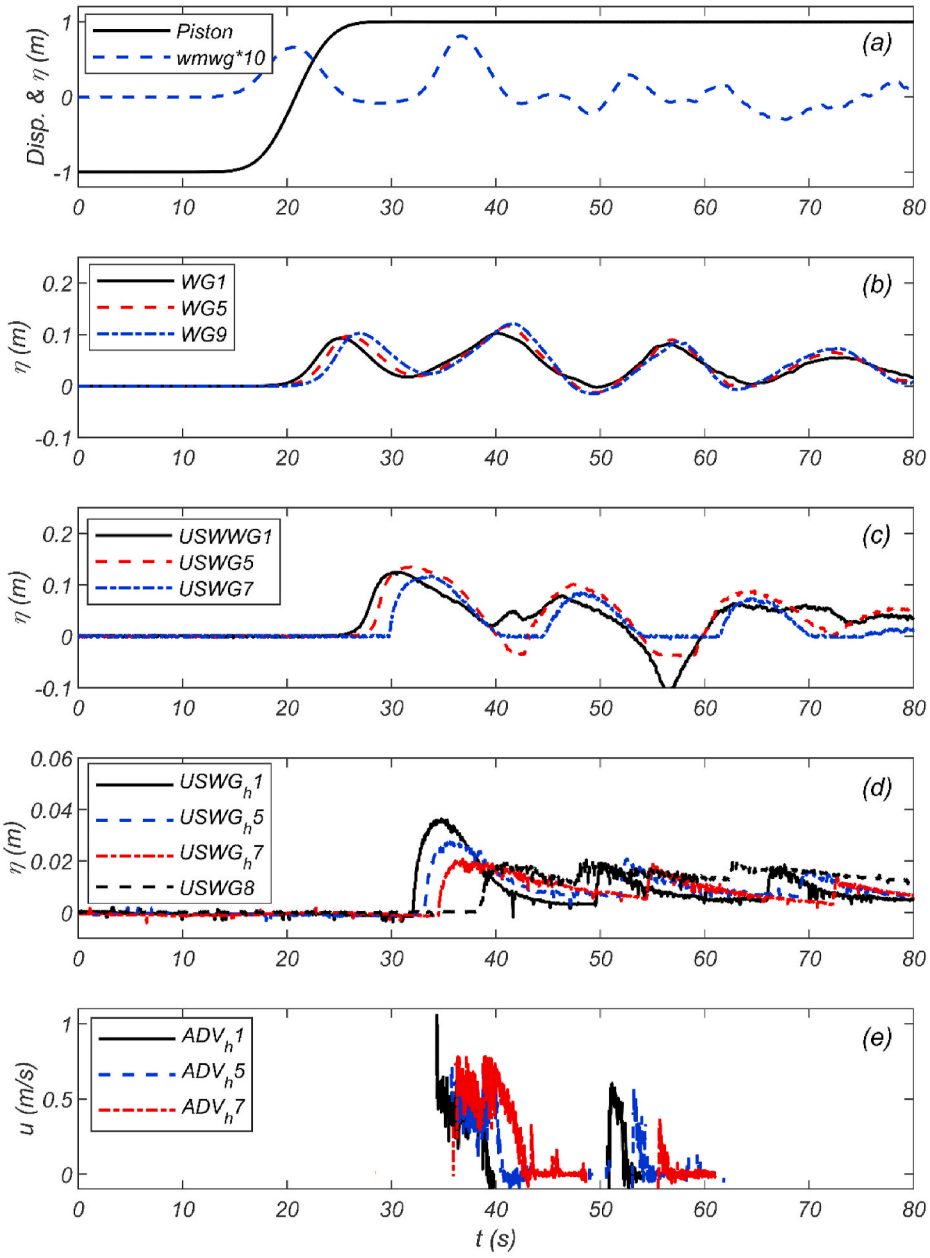

Fig. 4. Time series of (a) displacement of piston and surface elevation at the wavemaker, surface elevation over the slopes by (b) wire resistance wave gages (WG) and (c) ultrasonic wave gages (USWG), (d) surface elevation at the flat test region by ultrasonic wave gages ($USWG_h$), and (e) measured x-directional velocity at ADV_h.

transport could be affected by the number and arrangement of debris elements (e.g., Goseberg et al., 2016; Nistor et al., 2017b; Stolle et al., 2017). For example, the spacing between debris elements or the location of the debris field itself relative to the shoreline could also affect the debris transport phenomena. To decrease the number of permutations and to focus our study on debris density and obstacles, we chose to keep the number of debris elements constant ($N = 20$), while previous studies had utilized series of different number of debris up to eighteen as a grouped debris (Nistor et al., 2017). Twenty elements were seen as a reasonable number to have confidence in the measured mean locations and to reproduce debris-debris contact that could influence their trajectories and final locations. Further, we kept the initial location of the debris field fixed to allow comparison among trials and to avoid having to change the camera setup. The debris field location was chosen at the leading edge of the flat test section ($x = 31.29\ m$).

We kept the overall footprint of the initial debris field constant. For this, we utilized a 71.4 cm by 56.1 cm frame so that we could place a matrix of 5 × 4 debris elements with a gap spacing of $\alpha = 5.1$ cm between each element within this frame. The frame was removed prior to the start of the tests. With this frame, we used three configurations for the initial debris position: Uniform (C1), Checker (C2), and Random (C3) as shown in Fig. 5. The Uniform and Checker configurations had 4 rows and 5 columns and constant gap spacing (α). The Random configuration consisted of the 20 debris elements within the frame at irregular orientations and spacings between the debris. The Checker configuration was used only with an equal mix of 10 HDPE and 10 wood debris elements. The Uniform and Random configurations were used with different levels of mixed debris.

The 10 m wide test section allowed for two debris groups to be tested simultaneously without interference by the adjacent tests. This was based on a number of preliminary tests and confirmed by checking for bias in the results presented here. The two test sections are termed as

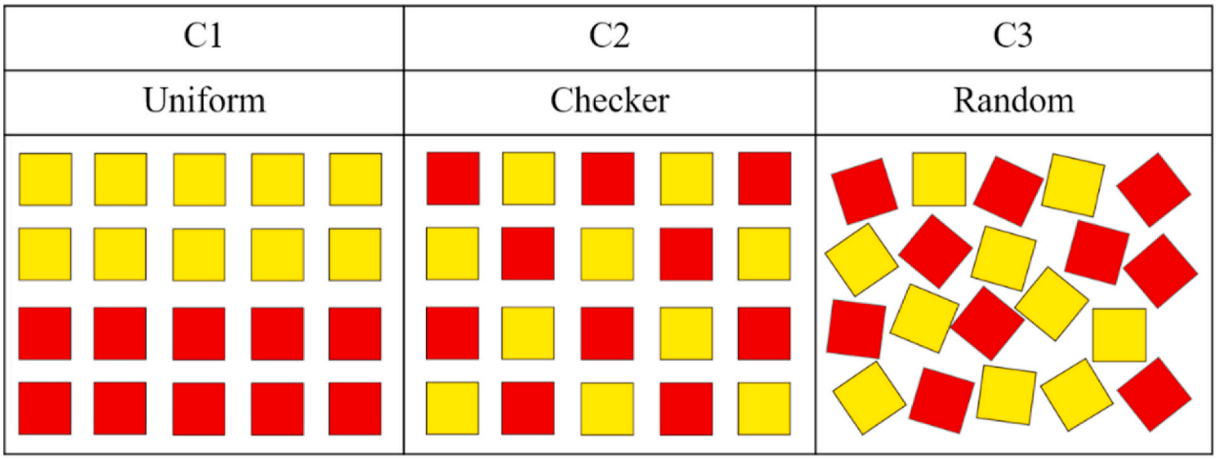

Fig. 5. Example sketch of three configurations of a debris group, C1 (uniform), C2 (checker), and C3 (random).

Region A and Region B, whose centroids are located at $y = -2.0\ m$ and $y = 2.0\ m$ as shown in Fig. 2b.

Table 3 summarizes the debris experiment cases, trials, and configurations. Column 2 denotes the debris configuration used, and Column 3 indicates the number of obstacles N_{obs} added in the test section. Cases 1–10 had no obstacles, and Cases 11–18 systematically increased N_{obs} in even increments from 2 to 6 for each region. Column 4 indicates the number of repeated trials for each case, N_r, and it is noted that not all trials could be repeated because of time constraints. In total, there were 45 trials conducted in two regions for a total of 90 tests. Column 5 shows the ratio of the gap distance to the characteristic debris length, a/L. Cases 1–4 were essentially pilot tests to determine whether this ratio had any effect on the overall tests, and it was observed that there was essentially no significant effect on the dislocation of debris for $0.25 < a/L < 2.0$. Therefore, $a/L = 0.5$ was used consistently for Uniform and Checker cases. The remaining columns show the number of HDPE and wood debris elements and the resulting specific gravity of the debris group SG_g in each region for each case. We considered debris groupings of 100% of one type, and mixes of 25%/75%, 50%/50%, and 75%/25% so that SG_g varied 0.65 (wood only), 0.74, 0.84, 0.91, and 0.99 (HDPE only). For example, Fig. 2b shows a trial for Case 16 with a Random (C3) configuration, 4 obstacles, and an equal mix of debris elements in Region A and B ($SG_g = 0.84$). The specific gravity (SG) represents the density (materials) condition of debris, and it is relatively convenient to be determined rather than the draft of debris, which is required to exact the shape (Volume) of debris. The grouped specific gravity (SG_g) could represent the effects of different density (materials) conditions on debris transportation as a group. Additionally, this dimensionless value is extendible to other applications such as the probabilistic approach on the multi-debris motions (interactions) or debris collision ratio to obstacles while debris transport as a group.

The fixed obstacles seen as gray boxes in Fig. 2b were 0.4 m by 0.4 m with 0.3 m height concrete blocks. The size of these obstacles was chosen to represent structures in the built environment such as commercial buildings that could affect the tsunami flow field. At a 1:50 geometric case, these obstacles would be 20 m wide in prototype, and the 400 m^2 prototype area is approximately the footprint of a popular US fast-food franchise or a small hotel. The row of obstacles was located 4 m from the initial debris field (200 m prototype) and could be considered a parking lot with passenger vehicles or container storage yard with shipping containers. The spacing between obstacles was 0.4 m (20 m prototype), the same as the length scale of the obstacles themselves. This facilitated the symmetrical placement of obstacles such that the case of $N_{obs} = 8$ obstacles had 12 total obstacles uniformly across Region A and B (note that 12 obstacles and 13 gaps at 0.4 m each equals the 10 m spacing of the test section). The middle four obstacles were common to both Region A and B.

Table 3
Description of debris experimental trials.

Case	Debris Config.	N_{obs}	N_r	α/L	Region A			Region B		
					HDPE (number)	Wood (number)	SG_g	HDPE (number)	Wood (number)	SG_g
1	C1	0	1	0.5	20	0	0.99	–	–	
2	C1	0	1	0.5	20	0	0.99	0	20	0.65
3	C1	0	1	2.0	20	0	0.99	–	–	
4	C1	0	1	0.25	20	0	0.99	–	–	
5	C1	0	2	0.5	15	5	0.91	5	15	0.74
6	C1	0	1	0.5	10	10	0.82	10	10	0.82
7	C2	0	1	0.5	10	10	0.82	10	10	0.82
8	C3	0	7	0.5	10	10	0.82	10	10	0.82
9	C1	0	2	0.5	5	15	0.74	15	5	0.91
10	C1	0	1	0.5	0	20	0.65	20	0	0.99
11	C3	2	4	0.5	20	0	0.99	0	20	0.65
12	C2	2	5	0.5	10	10	0.82	10	10	0.82
13	C3	2	7	0.5	10	10	0.82	10	10	0.82
14	C3	2	1	0.5	0	20	0.65	20	0	0.99
15	C2	4	1	0.5	10	10	0.82	10	10	0.82
16	C3	4	3	0.5	10	10	0.82	10	10	0.82
17	C2	8	3	0.5	10	10	0.82	10	10	0.82
18	C3	8	3	0.5	10	10	0.82	10	10	0.82

3.3. Correction and rectification of video images

Fig. 6a–d shows an example field of view from each of the four cameras for the same trial. To correct for lens distortion, we collected a number of black and white checkerboard images with a 0.1 *m* unit width throughout the test section. We utilized these images to extract the camera correction parameters using the 'undistortImage.m' provided in the camera calibration app from the Matlab toolbox and applied them to our raw recorded images. The estimated overall mean error was less than 3 pixels for all four cameras, which is equivalent to about 3 cm. After the lens correction, the images were rectified through 'fitgeotrans.m', which utilizes the surveyed locations of the orange gridline intersections on the test section. Finally, the four rectified images were merged and trimmed into a single image to cover the test region. Fig. 6e shows the example result for Case 6 with a uniform mix of debris (10 HDPE and 10 Wood) without obstacles. This was repeated for the final debris position for all trials for subsequent analysis in Section 4.1 and 4.2. For nearly all trials, this process was repeated frame-by-frame to provide continuous video for the debris velocity analysis in Section 4.3.

3.4. Optical measurement of debris transport

Fig. 7 shows a series of video images from Case 6. Debris groups in Region A and B use a uniform (C1) configuration with an equal mix of HDPE and wood elements. The initial debris configurations are slightly different with HDPE placed in the first and second rows in Region A and the third and fourth rows in Region B. At the time of $t^* = 9$ *s*, the leading edge of the tsunami-like wave reaches the initial debris field, and by $t^* = 19.0$ *s*, all debris has reached their final location. Here, t^* is the time frame corresponding to the video recording, where $t^* = 0$ is the manual start of the video recorder and corresponding to the wavemaker motion at $t = 16$ *s* in Fig. 4a. In general, the debris was entrained by the leading edge of the flow and started moving, initially dragging on the bottom until the flow depth was sufficient for the buoyant force to fully float the debris. Then the debris was transported smoothly over the testbed, although some debris-debris collision, subsequent dragging, and interactions were observed as will be described later. The white boxes indicate detailed regions shown in Fig. 8.

The effect of density can be seen in these images, where the less dense debris (wood, yellow) is transported much further in the flow direction (x-direction) over the test section. The major difference in the debris transport between two different debris elements is caused by the different draft conditions of HDPE (5.03 cm) and wood debris (3.30 cm) and relative flow depth changes over the testbed. As mentioned earlier, the HDPE debris is grounded earlier than the wood debris, and, consequently, the grounded HDPE disturbs the downstream flow fields and debris motions.

Although there is some variation among the final location for the ten elements of either density, there is almost no overlap among the debris types in the *x*-direction. Interestingly, although the initial placement of the debris elements was reversed in Region A and B, the sequence of images shows how the lighter density (yellow) objects move past the higher density objects in Region A around $t^* = 12$ *s*. By $t^* = 14$ *s*, all of the lighter density objects are further in the *x*-direction compared to the denser objects in Region A. These lighter objects are in a similar position to their counterparts in Region B, indicating the effects of the initial debris configuration are short-lived for these experiments.

Fig. 8 shows the details of the initial entrainment and transport process for Region A highlighted in the previous figure. Initially, as the tsunami reaches the debris field, the gaps between the debris are closed ($t^* = 9.5$ *s*). Five columns are formed and bend radially, matching more or less the radial wavefront seen in the images. This motion was also observed at a larger scale by Rueben et al. (2015) and by Nistor et al. (2017b). Ultimately, the columns become unstable ($t^* = 11$ *s*), beginning with the outer columns moving toward the middle column. This destabilization of the column is also observed in the uniform debris case, although the column becomes destabilized more quickly in the case of debris with uniform density. In any case, the lighter debris field moves through the heavier field ($t^* = 12$ *s* and 14 *s*). The light debris on the left-most column flows rather easily to the left of the two heavier debris pieces ahead (Fig. 8d), and a mirror image of that occurs on the right-most column. The light debris in the three middle columns experiences some debris-debris collision (Fig. 8e). Rather quickly, the debris fields become separated with the outer debris pieces moving much further along in the flow (Fig. 8f).

It is worth noting that not all debris elements moved with constant velocity for all tests, with some debris elements experiencing local acceleration or deceleration due to the local changes of flow field between

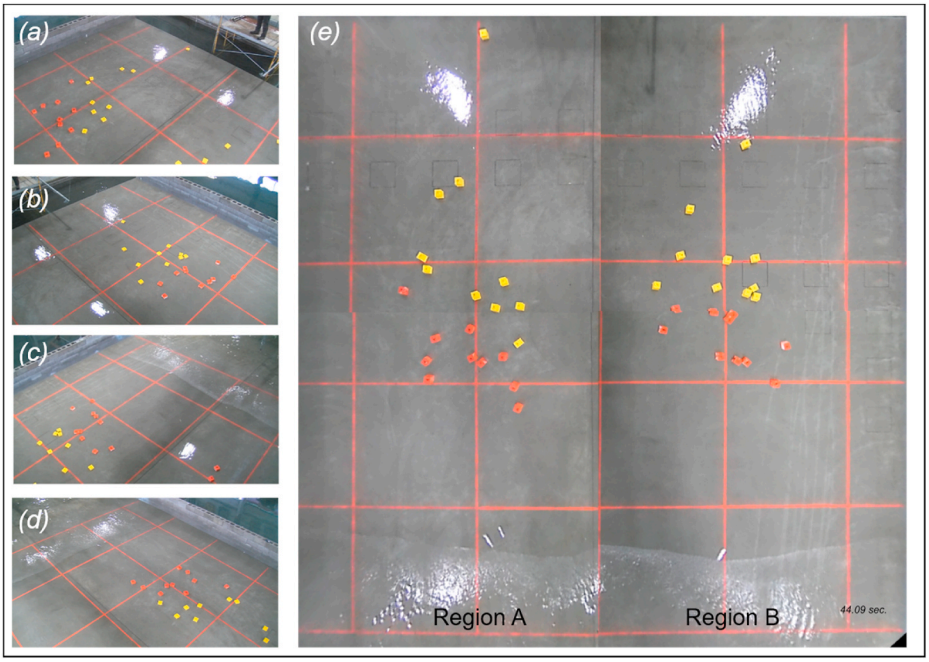

Fig. 6. Example snapshots of recorded video images of Case 6. (a) to (d) A raw video image from CAM1 to CAM4. (e) A rectified and merged image for Case 6.

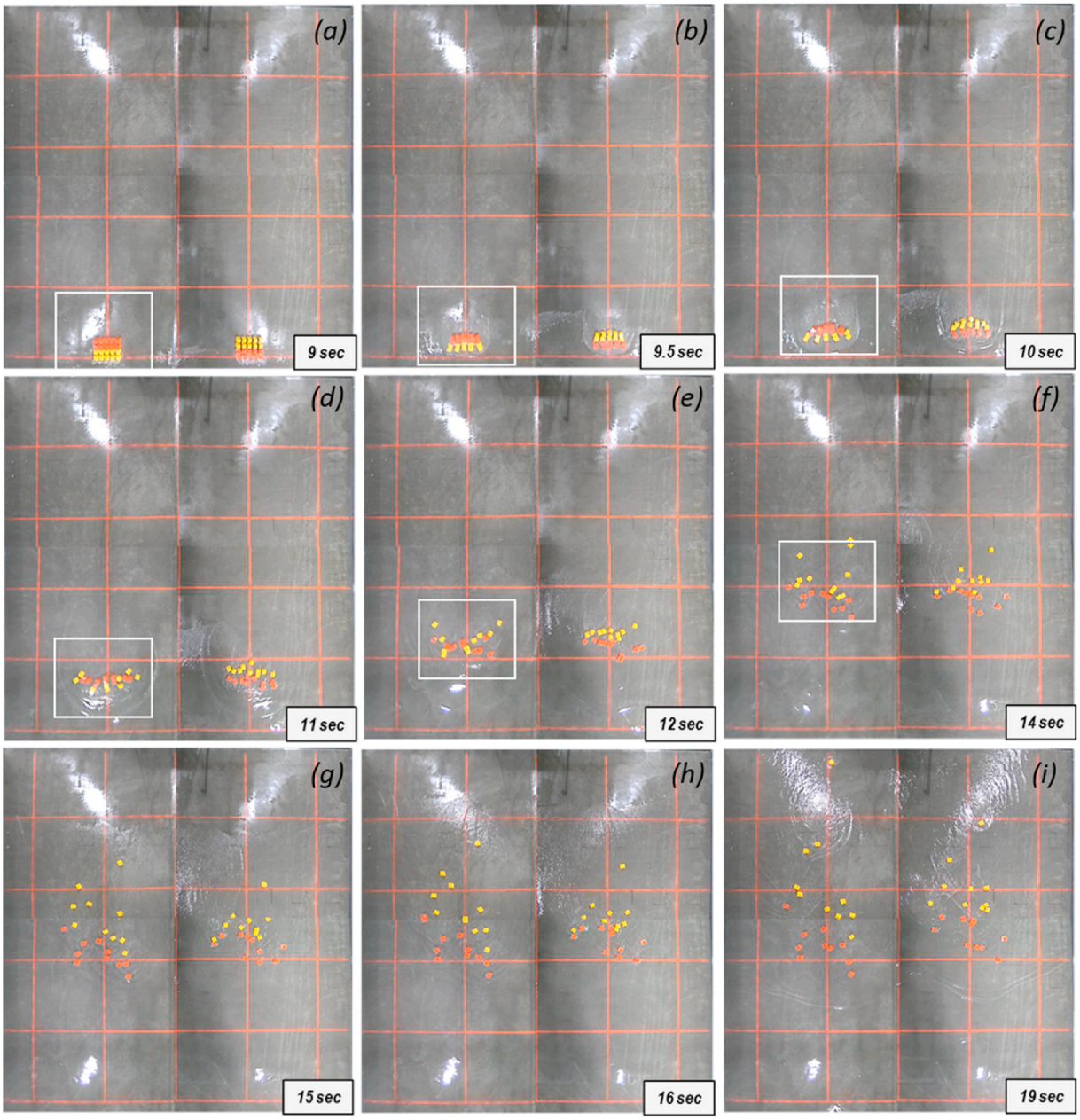

Fig. 7. Series of images showing debris entrainment and transport for Case 6.

adjacent debris, debris-debris collision, and interaction with the concrete floor with changes in flow depth. This was also observed by Rueben et al., (2015) (see, for example, their Fig. 13c) during some, but not all, of their repeated trials, suggesting that this temporary grounding may be due to slight variabilities in the flow field, particularly the wakes that are generated during debris entrainment. In general, though, the lighter (wood) moved more uniformly and much further in the *x*-direction when it was not impeded by heavier (HDPE) debris.

3.5. Quantification of final debris location

Fig. 9a and b shows the initial and final debris locations in Region A and Region B for the same case shown in Fig. 7 where the X' and Y' are the new Cartesian coordinates with the origin at the center of the debris frame ($x = 31.65\ m, y = -2.0\ m$ in Region A and $x = 31.65\ m, y = 2.0\ m$ in Region B). The final displacement of the *i-th* debris (D_i) and its spreading angle (θ_i) from the center of the debris frame was calculated. The red and black dashed lines indicate the mean longitudinal distance of HDPE and wood debris, respectively, which are calculated as

$$\overline{D'_X} = \left(\sum_i^n D_i \cos \theta_i \right) \Big/ n \tag{1}$$

where n is the total number of HDPE or wood debris elements used in each case. Comparing Region A and B, the mean longitudinal distance of HDPE and wood debris is not sensitive to the initial positioning of debris, even though the details of the entrainment and transport processes shown in Fig. 7 were different. In addition to the displacement, we used the video images to estimate the debris velocity in the X' direction across 100 cm intervals and marked them as *S1*, *S2*, *S3*, *S4*, *S5*, and *S6* in Fig. 9b.

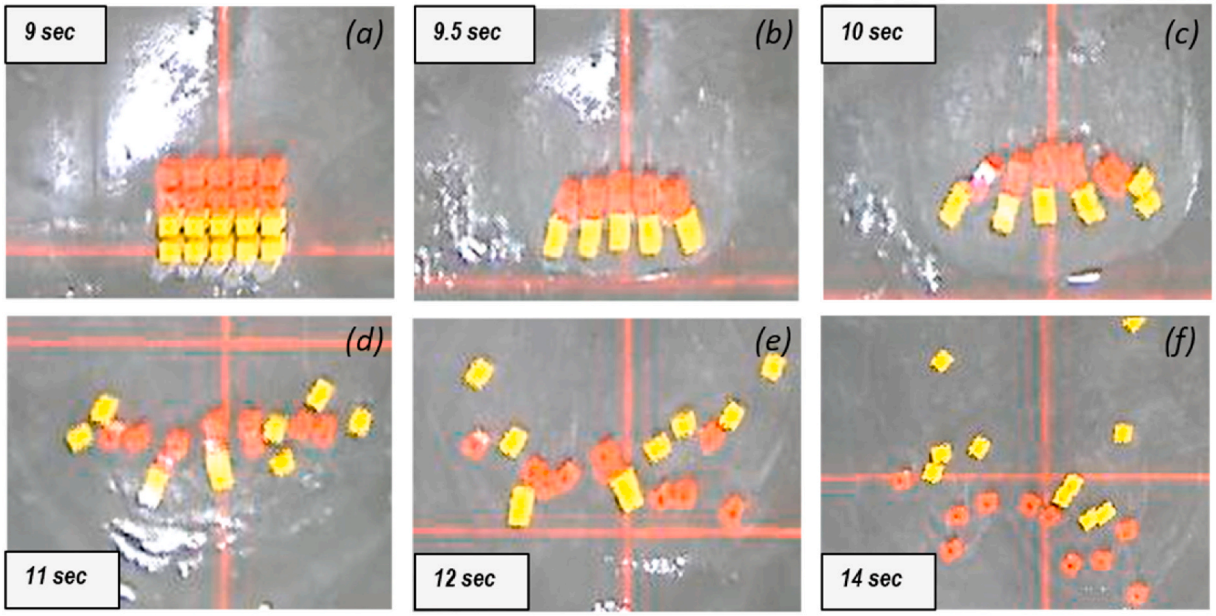

Fig. 8. Detail from Fig. 7 of the entrainment and transport process in Region A.

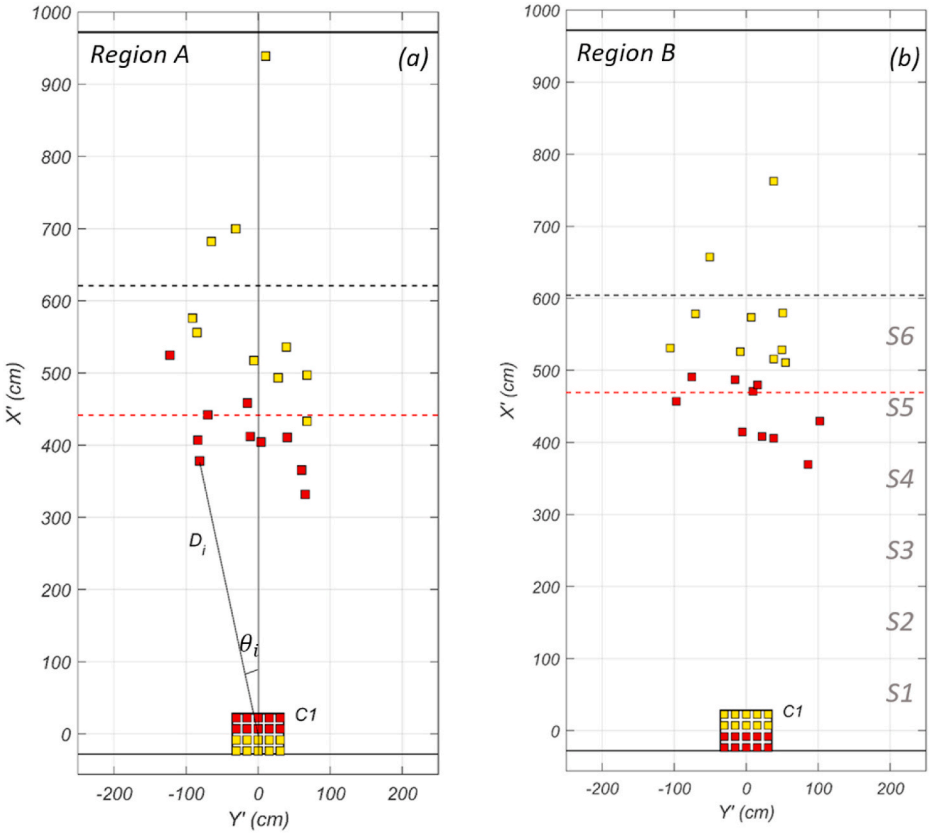

Fig. 9. Digitized results of the case with $SG_g = 0.82$ (Case 6, Fig. 7) at initial debris position ($t^* = 0\ s$) and the final stage ($t^* = 19\ s$). (a) at Region A, and (b) at Region B. The red and yellow square indicates the location of HDPE and wood debris, respectively, and red and black dashed lines indicate the mean longitudinal distance of HDPE and wood debris, respectively. (For interpretation of the references to color in this figure legend, the reader is referred to the Web version of this article.)

4. Results of debris advection

4.1. Longitudinal distance of debris

Fig. 10 shows the results of two different SG_g conditions with two different initial positions of HDPE and wood in Region A and B. The upper panels (Fig. 10a, b, c, d) present the case of SG_g is 0.91 (Case 5) composed of 15 HDPE and 5 wood elements, and the lower panels (Fig. 10e, f, g, h) present the case of SG_g is 0.73 (Case 9) with 5 HDPE and 15 wood elements. The tests utilized the Uniform (C1) configuration,

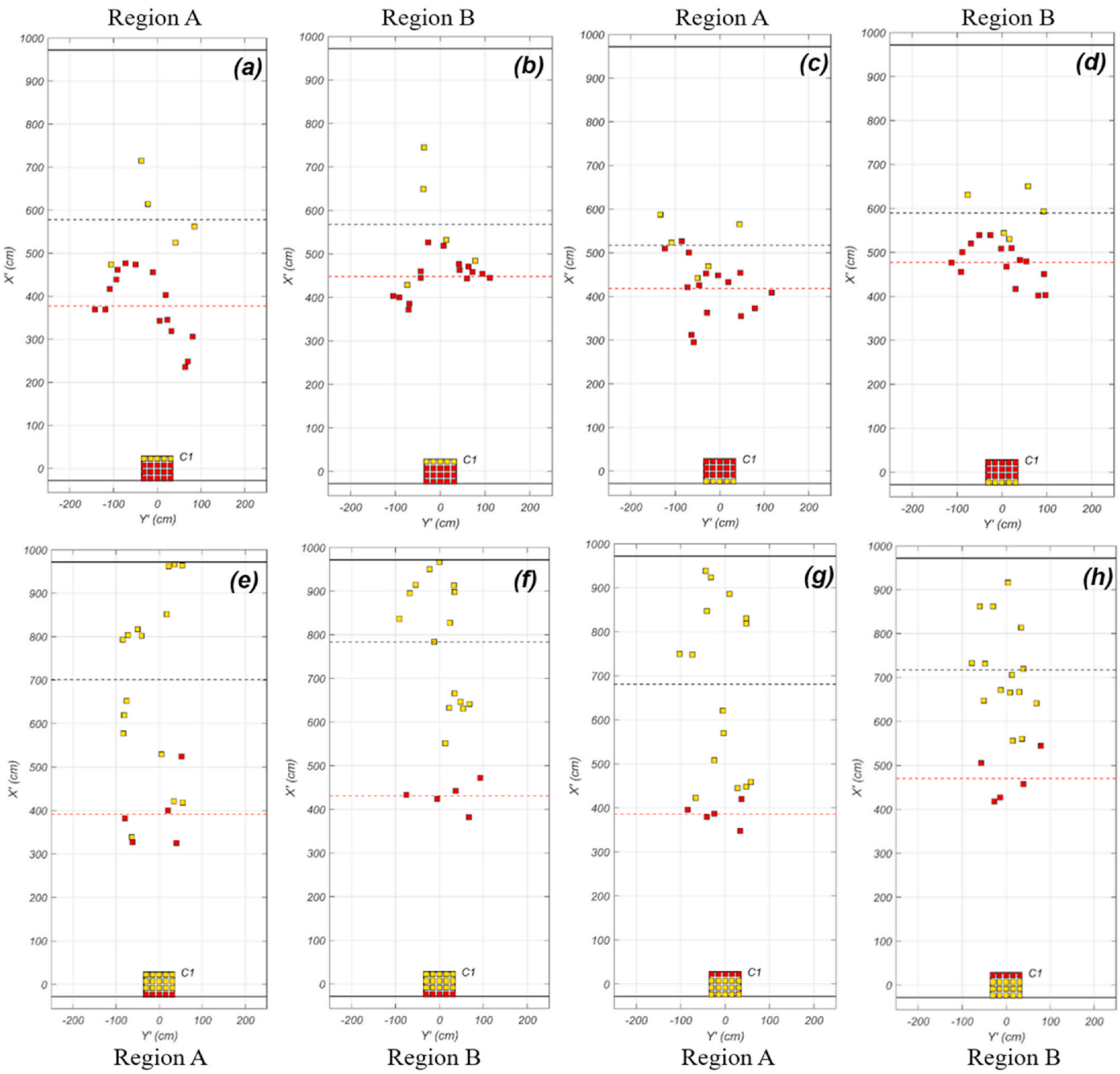

Fig. 10. Initial and final debris locations for Case 5 (upper panels) and Case 9 (lower panel). (a) to (d) present 15 HDPE and 5 wood elements (Case 5) with different initial debris configuration and at two different regions (Region A and B). (e) to (h) present 5 HDPE and 15 wood elements (Case 9).

and the left four panels (Fig. 10a, b, e, f) present cases where the wood debris is landward of the HDPE, while the right four panels (Fig. 9c, d, g, h) present the opposite case of the wood on the seaward side of the HDPE. Lastly, the same initial debris positions are repeated at each Region A (Fig. 10a, c, e, g) and Region B (Fig. 10b, d, f, h).

For the top panels (Fig. 10 a, b, c, d), the mean longitudinal distance ($\overline{D_x'}$) of the wood debris ranges from 510 to 590 cm and is approximately 31% further than the HDPE debris elements in the range 390–480 cm. For the bottom panels (Fig. 10 e, f, g, h), $\overline{D_x'}$ of the wood, debris elements range from 690 to 790 cm and are approximately 72% further than the HDPE in the range 390–470 cm. Two major observations can be made. First, as was noted in Fig. 7, $\overline{D_x'}$ is independent of the initial orientation of the debris: whether the wood debris was landward or seaward of the HDPE did not affect $\overline{D_x'}$ for a given SG_g condition. Second, while there was a significant change in $\overline{D_x'}$ for the wood debris due to different SG_g conditions, there was no significant change in $\overline{D_x'}$ for the HDPE debris. In other words, $\overline{D_x'}$ was much larger for the wood debris when the group consisted of 75% wood debris compared to 25% wood debris, but $\overline{D_x'}$ was about the same for 75% HDPE as it was for 25% HDPE.

To generalize the effects of group density on the longitudinal distance, Fig. 11 shows the mean longitudinal distance and the 95% of confidence interval for HDPE and wood debris for the five SG_g conditions from $SG_g = 0.65$ (wood only) to $SG_g = 0.99$ (HDPE only). For comparison, we plot $\overline{D_x^*}$ defined as the mean longitudinal distance normalized by the mean longitudinal distance of Case 8 with $SG_g = 0.82$ (equal number of HDPE and wood elements) and Random (C3) debris configuration. Case 8 was repeated seven times (Table 3), and the values used for normalization were $\overline{D_x'} = 4.51\ m$ for HDPE and $\overline{D_x'} = 6.99\ m$ for wood.

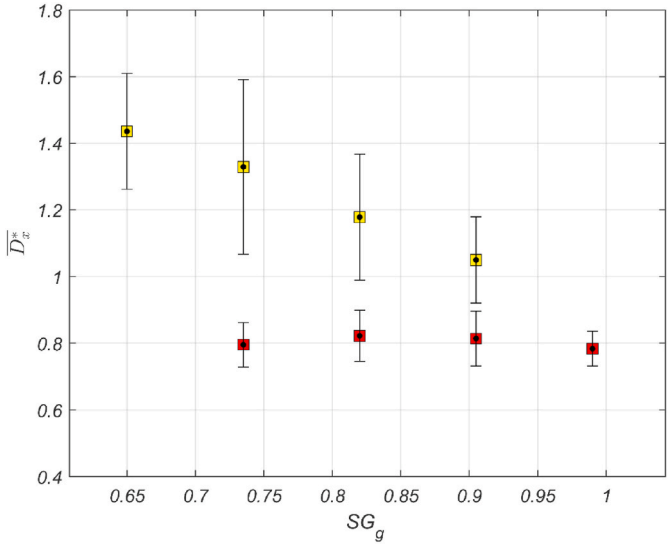

Fig. 11. Normalized mean longitudinal distance, $\overline{D_x^*}$ of HDPE and wood and debris as a function of SG_g. Vertical bars indicated a 95% confidence interval.

It is noting that seven repeated trials only intended to check the repeatability of our experimental procedure. Fig. 11 clearly shows that $\overline{D_x^*}$ for the higher density debris (HDPE, red) is nearly constant ($\overline{D_x^*}$ ~0.8) while $\overline{D_x^*}$ for the lower density debris (wood, yellow) decreases linearly as SG_g increases. This linear decrease would extrapolate to approximately the same value of $\overline{D_x^*}$ for the HDPE only case.

It is interesting to note that the variation in $\overline{D_x^*}$ indicated by the 95% confidence limits (c.l.) are fairly uniform across all values of SG_g for HDPE, indicating that the presence of the lighter debris has little to no influence on the heavier debris. Moreover, the 95% c.l. is several times smaller than for the wood debris. On the other hand, the 95% c.l. for the wood debris increases as SG_g decreases, indicating that the presence of the heavier debris affects the variability in the final position of the lighter debris. Even a relatively small amount of heavier debris (25%) causes the variation in $\overline{D_x^*}$ for the lighter debris for $SG_g = 0.73$ cases to be larger than the cases where only the lighter debris was present (SG_g = 0.65).

4.2. Spreading angle of debris

The spreading angle of debris is a key variable to estimate the region for potential tsunami debris impacts or debris damming from the initial debris site (e.g., ASCE, 2016). Based on a field survey from the 2011 Tohoku tsunami of debris from a shipping container yard, Naito et al. (2014) estimated the debris spreading angle as

$$\theta = \pm 22.5^{\circ} \tag{2}$$

where $\theta = 0^{\circ}$ is defined perpendicular to the shoreline, and it was assumed that the tsunami inundation was also normally incident to the shoreline. Nistor et al. (2017b) conducted a small-scale physical model study, suggesting that the debris spreading angle increases as the number of debris elements increases. They found that

$$\theta = \pm 3.69^{\circ} \pm 0.80\,N \tag{3}$$

where N is the number of debris elements.

Fig. 12 shows the spreading angle for all trials for Cases 1, Case 4 – Case 10 computed using Eq. (2), and Eq. (3) ($N = 20$, $\theta = \pm 19.69^{\circ}$). The denser debris (HDPE, red) shows a wider spreading angle and is bounded reasonably well by both equations. However, the less-dense debris (wood, yellow), which has a shallower draft (3.30 cm), has a narrower spreading angle, $\theta = \pm 11^{\circ}$, compared to the denser debris, which has a deeper draft (5.03 cm), highlighting the role that debris density could have in debris dispersion. Moreover, Fig. 12 shows that both equations are conservative in their estimates of debris spreading angle for the less dense debris.

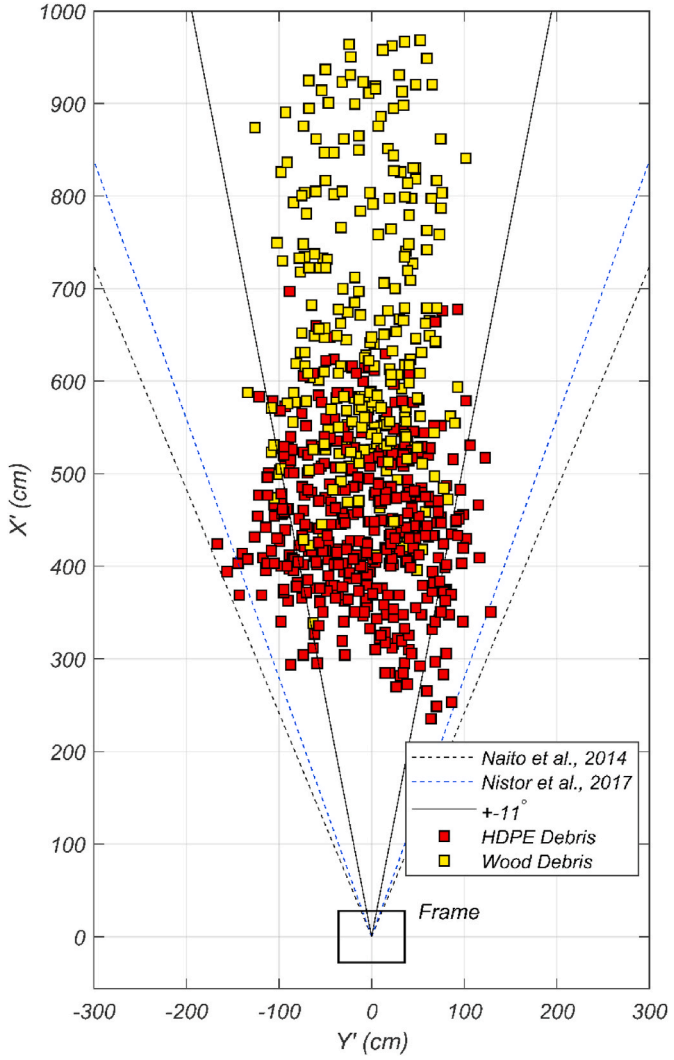

Fig. 12. Coordinate of debris from all trials for Case 1, 4 to 10. The solid box indicates that the frame we used for the initial position setup of debris. Each black and blue dashed line indicates the Spreading angle predicted by Eq. (2) (dashed black, Naito et al., 2014), Eq. (3) (dashed blue, Nistor et al., 2017b), and ±11° (solid black). (For interpretation of the references to color in this figure legend, the reader is referred to the Web version of this article.)

Fig. 13 shows the spreading angle of wood (Fig. 13a) and HDPE (Fig. 13b) debris at the five SG_g conditions. In the figure, each colored box indicates the spreading angle (θ_i) of a single debris element in a given trial at that SG_g condition, the black line shows the mean spreading angle across all trials, and a blue box indicates the 95% confidence interval, q_{95}. Overall, the spreading angle of wood debris is narrower than the predictions of Naito et al. (2014) and Nistor et al. (2017b) and is typically less than 10°. Overall, the spreading angle increases slightly for the less dense debris as SG_g condition increases.

Fig. 13b for the HDPE debris shows a somewhat clearer trend of the spreading angle increasing as the SG_g condition increases. In any case, there is a clear distinction in the spreading angle for the wood only case ($SG_g = 0.65$, $-8^{\circ} < q_{95} < 10^{\circ}$) and the more dense HDPE cases (SG_g = 0.99, $-22^{\circ} < q_{95} < 20^{\circ}$).

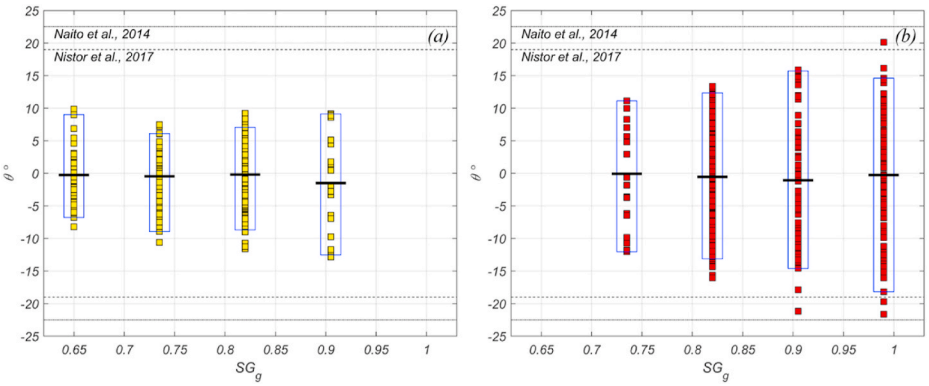

Fig. 13. Spreading angles of (a) wood debris and (b) HDPE debris at different SG_g conditions.

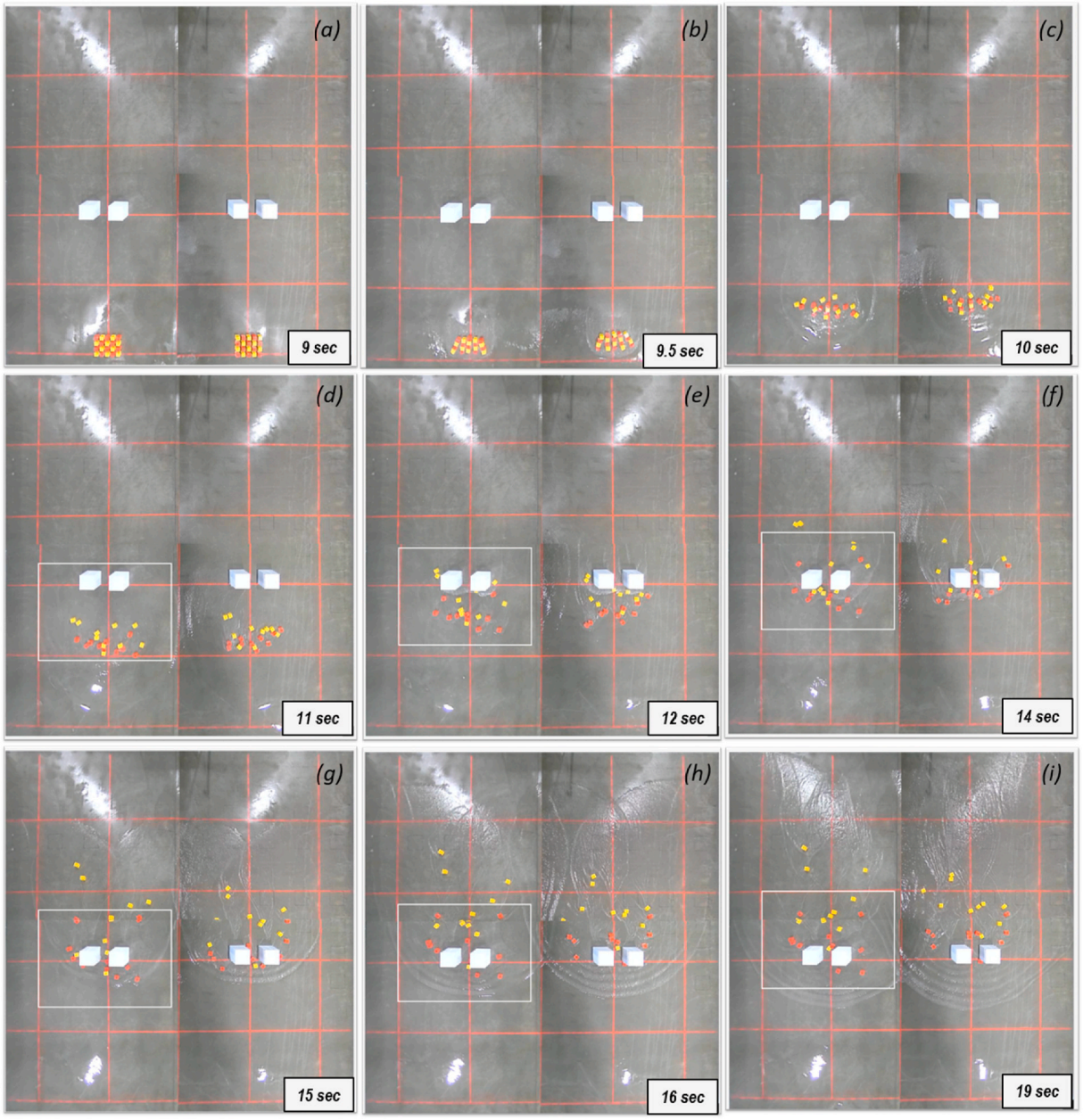

Fig. 14. Snapshot of a series of the rectified image with $N_{obs} = 2$ (Case 12).

5. Results of debris advection with obstacles

Macro-roughness conditions provided by buildings or other structures strong enough to withstand the hydrodynamic tsunami forces can significantly alter the flow dynamics (e.g., Park et al., 2013; Goseberg, 2013; Tomiczek et al., 2016; Qin et al., 2018; Winter et al., 2020), but the effects of those obstacles on the debris advection are not understood yet clearly. In particular, the characteristics of flow fields and debris transport are altered by the characteristics of obstacles, such as size, shape, position, and geometry, and position of the obstacles. As described earlier in reference to Table 2, we tested debris advection with obstacles in a relatively simple manner by the systematic addition of box-shaped obstacles at a fixed distance landward of the debris field.

Analogous to Figs. 7 and 14 shows a series of video images from Case 12 (N_{obs} = 2, SG_g = 0.82, C2 (Checker) configuration), and the white boxes indicate details shown in Fig. 15. The leading edge of the tsunami-like wave reaches the test sections at t^* = 9 s (Fig. 14a), and the debris initially forms radial columns at t^* = 9.5 s (Fig. 14b). At t^* = 10 s, the columns are no longer visible, and the debris is still well-mixed (Fig. 14c). By t^* = 11 s, sorting of debris is visible with the less dense debris (wood, yellow) leading most of the denser debris (Fig. 14d). In the remaining frames, the debris can be seen to interact with the obstacles with some of the debris flowing between and around the obstacles. Some of the debris elements were seen to make contact with the obstacles. Starting at t^* = 14 s and continuing to t^* = 19 s, the leading wave is partially reflected from the obstacles, and this reflection resulting in a raised water levels in front of the obstacles affected the debris trajectories.

Fig. 15 shows the series of detailed images from Fig. 14 in the vicinity of the obstacles for t^* = 11, 12, 14, 15, 16, and 19 s. Initially, the reflection developed at the front of an obstacle before the approach of debris (Fig. 15 b). The reflection decelerated most of the debris motion nearby the obstacles and changed debris trajectories around obstacles, while some of the debris collided into the obstacles (Fig. 15c). Debris passed between obstacles at relatively low speed (Fig. 15d), and the debris accelerated as it passed between obstacles due to the wake developed behind of obstacles (Fig. 15e). Most of the debris elements that collided with the obstacles eventually passed between obstacles (Fig. 15f). Overall, an inspection of these figures shows interesting features described above, including the sorting of debris by density, the collision of debris with the obstacles, the flow through and around obstacles, and the reflected wave developed from the obstacles that interfered with the debris.

5.1. Effects of obstacles on spreading angle and longitudinal distance

Fig. 16 shows the final locations of HDPE and wood debris for the three conditions of N_{obs} = 2, 4, 8. Fig. 16a includes Case 11 to Case 14 with C2 (checker) and C3 (random) configurations with three SG_g conditions (SG_g = 0.65, 0.82, and 0.99). Fig. 16b and c includes C2 (checker) and C3 (random) configurations with SG_g = 0.82 only. Similar to Fig. 12 with no obstacles, Fig. 16 shows that the less dense debris travels farther than the denser debris even with the presence of obstacles. The introduction of the two obstacles has a significant effect on the spreading angle and longitudinal distance relative to the no obstacle case (Fig. 12). Somewhat surprisingly, however, the spreading angle and longitudinal distance are not significantly affected by the increasing number of obstacles, suggesting that there is a fairly narrow lateral limit to the effect that obstacles can have on debris transport.

17 shows the mean normalized longitudinal distance $\overline{D_x^*}$ and 95% confidence intervals for HDPE and wood debris for the cases with obstacles for SG_g = 0.82, including the case of no obstacles from Fig. 11. The two horizontal dashed lines indicate the location of the lower and upper edge of obstacles. Fig. 17 shows a significant decrease in $\overline{D_x^*}$ for the less dense debris from N_{obs} = 0 to N_{obs} = 2 obstacles and then a constant $\overline{D_x^*}$ as N_{obs} increased. The 95% confidence limit also decreases from N_{obs} = 0 to N_{obs} = 2 obstacles. The dense debris, however, does not show a change in $\overline{D_x^*}$ or 95% confidence limit as N_{obs} increases, even between the N_{obs} = 0 and N_{obs} = 2 cases.

To evaluate the potential change in spreading angle under different SG_g conditions with obstacles, we analyzed our results similar to that shown in Fig. 13 and, for brevity, our results are summarized in Table 4 which lists the spreading angle based on the 95% exceedance, q_{95}, for the left and right directions and the different SG_g conditions. The far-right column lists the mean absolute value for both directions and all SG_g conditions, $|q_{95}|_{\text{mean}}$. In general, the mean spreading angle of the higher density debris (HDPE) was larger than the lower density for both cases of with and without obstacles. The presence of obstacles increased the spreading angle for both debris types. These finding is contradictory to the previous observation, which showed lower spreading angles with the presence of obstacles to the downstream (Goseberg et al., 2016). The

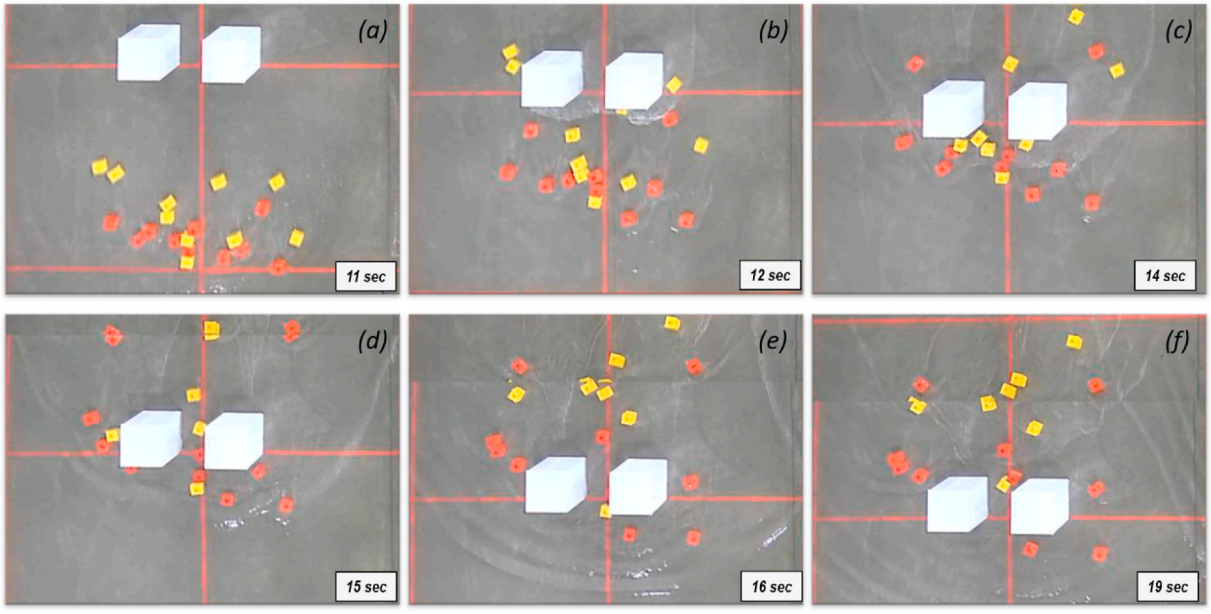

Fig. 15. Series of detailed images near obstacles for Case 12 in Region A.

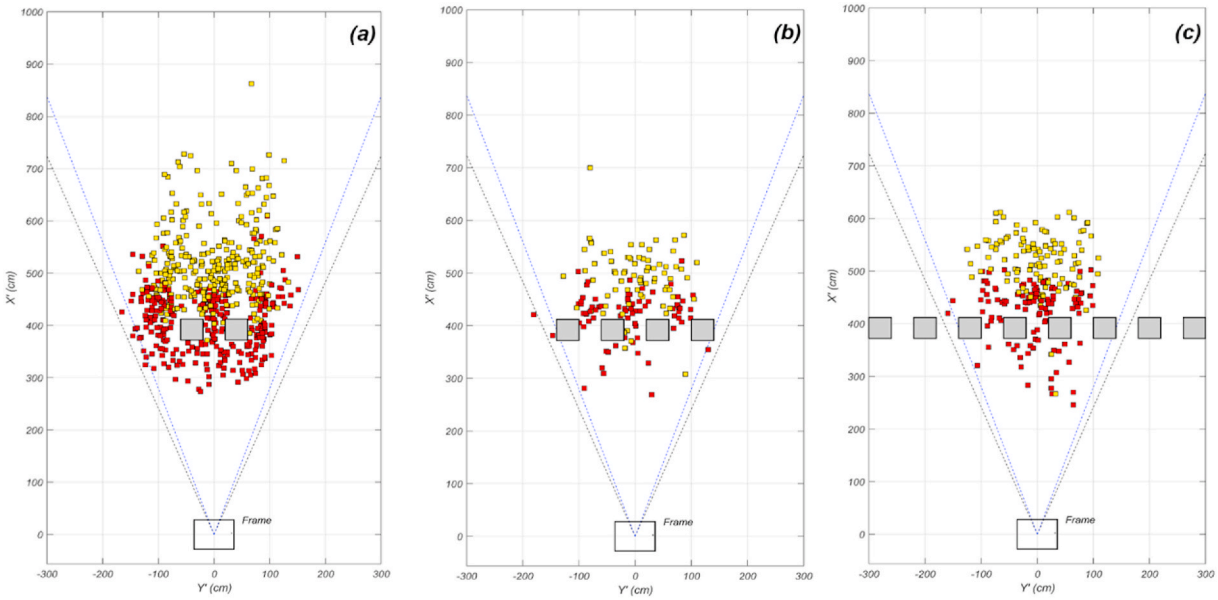

Fig. 16. Final location for debris for three different obstacle cases: (a) Case 11–14 with $N_{obs} = 2$, (b) Case 15–16 with $N_{obs} = 4$, (c) Case 17–18 with $N_{obs} = 8$.

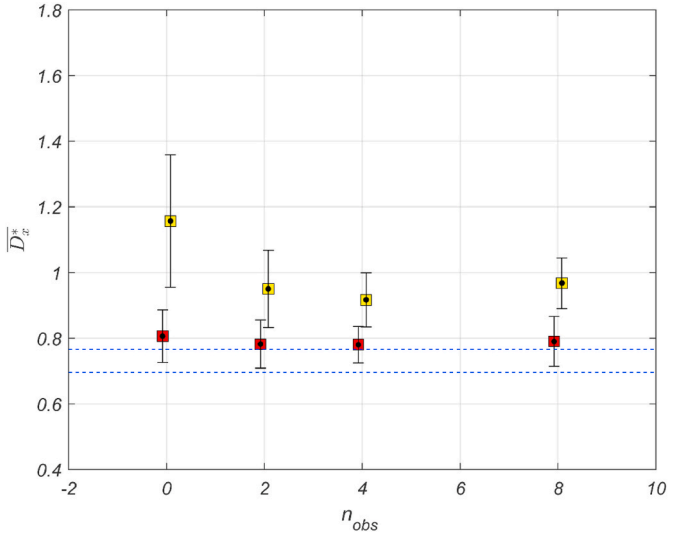

Fig. 17. Longitudinal distance $\overline{D_x^*}$ with a different number of obstacles N_{obs}. Blue dashed lines indicate the lower and upper edge of obstacles. (For interpretation of the references to color in this figure legend, the reader is referred to the Web version of this article.)

flow fields over obstacles and corresponding debris transportation are significantly altered by the geometry of obstacles (location, size, and gap) and debris size, number, and configurations). For example, the relative length scale of debris to obstacle (L/L_{obs}) in our study was 0.25, while it ranged about 0.5–2.0 in Goseberg et al. (2016). Furthermore, the different tsunami inputs, flow fields (e.g., Froude number, and duration), different ratio of flow depth to draft, and different number of debris conditions will result in large variation in spreading angles.

5.2. Debris collision with obstacles

The video images similar to those shown in Fig. 14 were inspected to identify debris element collision with obstacles. Debris is classified as a collision case if debris is partially collided with obstacles and changed its moving direction. Fig. 18a shows the total ratio of a collision of debris at three different SG_g conditions ($SG_g = 0.62$, 0.82, and 0.99) with standard deviations. Not all HDPE debris reached to obstacles and we excluded this debris to calculate the ratio of collision. There is a relatively high collision probability for $SG_g = 0.62$ (wood only) and a lower collision probability at $SG_g = 0.99$ (HDPE). This is perhaps counter-intuitive because it was initially thought that the higher density debris would have larger inertia and therefore would continue its trajectory into the obstacle. However, this was not the case, and it was observed that the wood debris element reaches the obstacle before the reflected wave was fully developed which may explain the observed differences. It might be a probability of grounding, depending on the individual draft of HDPE and wood debris. Therefore, we can expect that if we test the debris collision for different obstacle locations over different flow depth conditions, the collision probability trend would be different. This may also explain why the spreading angle of wood debris is relatively narrower than HDPE as shown in Table 4.

Table 4
Summary of spreading angles based on 95% exceedance (q_{95}) with and without obstacles.

Debris type	N_{obs}	Orientation	q_{95}					$\lvert q_{95}\rvert_{mean}$
			$SG = 0.62$	0.73	0.82	0.91	0.99	
wood	0	Left	−6.8°	−8.9°	−8.7°	−12.5°	n/a	8.5°
		Right	9.0°	6.1°	7.1°	9.1°		
	2	Left	−10.7°	n/a	−12.8°	n/a	n/a	11.6°
		Right	11.1°		11.8°			
HDPE	0	Left	n/a	−12.0°	−13.1°	−14.6°	−18.2°	14.0°
		Right		11.1°	12.4°	15.7°	14.6°	
	2	Left	n/a	n/a	−15.7°	n/a	−20.9°	17.4°
		Right			15.7°		17.3°	

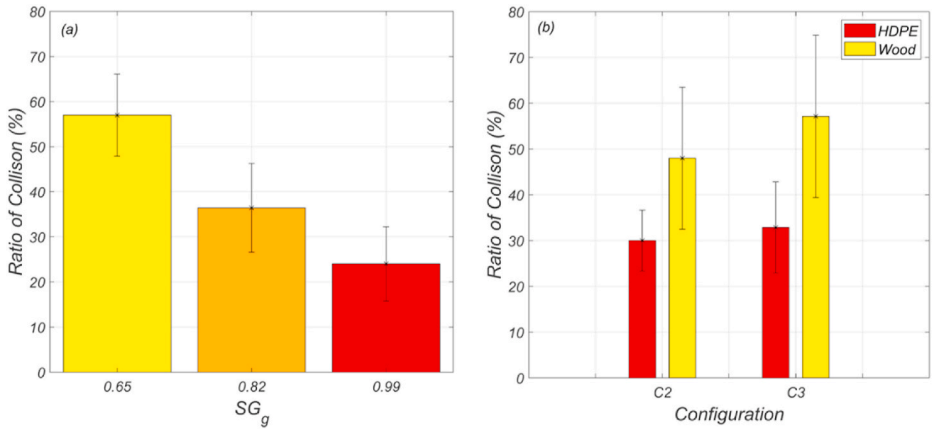

Fig. 18. Collision ratio according to HDPE rate and initial arrangement of debris.

Fig. 18b disaggregate the results of the $SG_g = 0.82$ cases by plotting the collision ratio separately for HDPE and wood and also distinguish between the initial configurations, C2 (Checker) and C3 (Random). Fig. 18b shows that there is a clear distinction in the collision ratio, even when the debris types are mixed. The initial configuration (Checker vs Random) does not seem to have had a strong effect.

5.3. Debris velocity with and without obstacles

As mentioned in the context of Fig. 9, we use the optical measurements to estimate the mean *u*-velocity (*x*-direction) of the leading-edge flow and individual debris elements at sections S1 to S6 identified in Fig. 9. Fig. 19 shows the mean *u*-velocity of the leading-edge flow (blue), wood (black), and HDPE (red) debris at the six sections (S1 to S6) at 100 cm intervals along the *x*-direction. The dashed and solid lines indicate cases with obstacles and without obstacles, respectively. The centroid of the initial debris field is at $X' = 0$, and the obstacles are centered at $X' = 397$ cm.

The mean velocity of leading-edge flow is nearly uniform for all sections from S1 to S6, increasing slightly from S1 to S2, remaining constant from S2 to S4, and decreasing slightly from S4 to S6. The leading-edge velocity is nearly the same for both cases, with and without obstacles, from S1 to S4 as expected and then is lower in the lee of the obstacles.

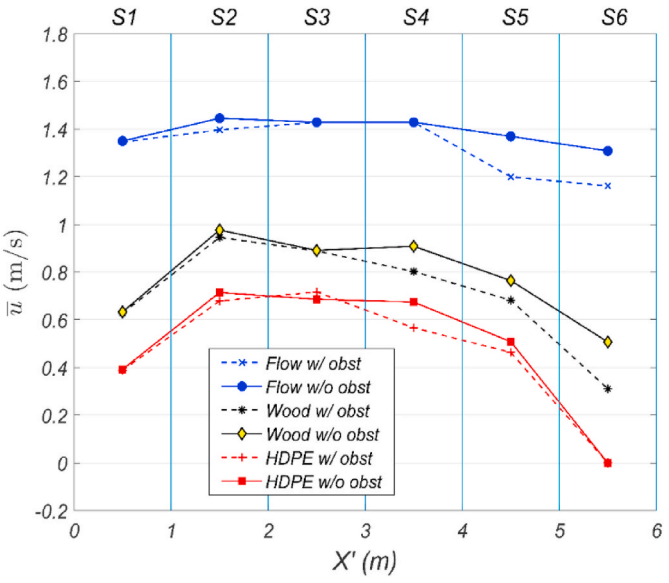

Fig. 19. Mean u-velocity of leading-edge and HDPE and wood debris with and without obstacles.

The velocity of the two debris types is lower than the leading edge velocity, with the wood debris reaching 70% of the leading edge velocity at S2 and the HDPE debris reaching 50% at S2. The velocity of the two debris could not reach the leading edge velocity because of relatively short moving distance and lower flow depth than the draft of each debris elements. To be specific, the maximum flow depth from S2 to S6 ranged from approximately 4 cm ($USWG_h1$) to 1 cm ($USWG_h7$) from Fig. 4d, while the draft of HDPE and wood is 5.03 and 3.30 cm. The velocity trends between the wood and HDPE are qualitatively similar from S1 to S3, and the HDPE reaches only about 70% of the wood debris velocity in these regions.

At S4, there is a clear decrease in the velocity of both debris' types just seaward of the obstacles relative to the cases without obstacles. This is a significant result because it shows that the presence of obstacles affects the velocity of the debris field. In some cases, individual debris elements were observed to reach very low velocities even though they did not directly collide with the obstacles. This decrease was often due to the reflected wave on the seaward side of the obstacle.

At S5 and S6 on the landward side of the obstacles, the wood debris velocity continues to be less than the velocity measured when no obstacles were present. On the other hand, the HDPE debris has only a very modest decrease in velocity at S5. At S6, the velocity is zero because the HDPE did not travel to this section as was shown in Fig. 16.

6. Discussion

This study provides a unique experimental analysis of debris advected by a transient flow over a flat testbed considering obstacles, representing an idealization of vehicles or shipping containers that would spread past buildings during a tsunami or hurricane surge event. The current study evaluates the sensitivity of the final longitudinal (inland) distance and spreading angle of debris transport due to the differences in debris density and initial conditions. The results highlight that there is little effect of the initial conditions (i.e., the position of higher or lower density elements within the initial field did not influence their final location or spreading angle). However, there was a significant effect of density on the final location and spreading angle and the collision probability of debris with obstacles. The specific ratio of relative flow depth to the draft of each debris, and corresponding debris motion changes including grounding and wakes, should be quantified to address the effects of density more clearly on debris transportation in the future.

Because these experiments were conducted at scale, we suggest a bit of caution in interpreting the results. First, we observed about 10 s of inundation, which at 1:50 scale assuming Froude similitude would correspond to 1.2 min in prototype conditions. This is much smaller than

the typical tsunami inundation time (10–30 min) observed for large tsunamis (e.g., Fritz et al., 2012). In any case, our observed differences in the landward extent due to debris density would also be relevant over longer inundation durations.

A second idealization for these experiments involved the use of a flat slope for the test section. This slope was utilized because the tests were conducted as part of a larger project for which the flat slope was designed such that the water flowed over the flat section into a stilling basin on the landward. The flat slope simplified the tests to some degree: the motion of the debris particles was laterally and in the onshore direction only. The debris never went seaward. This is in contrast to debris movement observed in the field where there can be seaward directed debris during the drawdown. Moreover, this is in contrast to the laboratory observations of Rueben et al. (2015). Even though they had used a flat test section, their experimental design did not allow for the overland flow to continue into a stilling basin. Instead, the flow was reflected from the back wall and returned seaward, bringing the debris elements seaward, often to a point more seaward than the initial starting location (see, for example, Fig. 12b in Rueben et al., 2015). Therefore, the importance of the return flow has not been considered in these tests. It is likely that bathymetric and topographic features would further complicate the tsunami inundation and subsequent overland flow and should be considered in future studies.

A third idealization involves the use of obstacles to represent the built environment. While the overall length scale of the obstacles was chosen to correspond to buildings, the number and arrangement of obstacles (N_{obs} = 2, 4, 8) and the spacing between the obstacles were chosen to simplify the testing and to allow for comparison between Region A and B. In general, our tests showed that there is a limit to the lateral influence of the obstacles. Fig. 17, for example, show essentially no difference in the mean longitudinal displacement $\overline{D_x^*}$ as the number of elements increases beyond $N_{obs} = 2$. However, this result may be for this location only, and if the obstacles were placed at a more landward distance, it is possible that $\overline{D_x^*}$ would be more sensitive to N_{obs}. Perhaps more importantly, the obstacles were only aligned laterally. In other words, it would have been possible to use other arrangement obstacles (for example in staggered rows and columns) that would have had a larger effect on the flow field and resulting debris trajectories (Goseberg et al., 2016). Finally, the relative length scale of the debris elements to obstacles (1:4) was kept constant using the uniform size of debris. The interaction of debris to obstacles and debris damming on obstacles will be sensitive to the number and shape (or size) of debris too (Stolle et al., 2018a). Future studies should consider how these geometry conditions of debris and obstacles affect the likelihood of impact and damming or change in debris flow velocity.

We acknowledge that the work presented in this study represents a small subset of debris inundation under idealized conditions. However, we anticipate that this work will be useful to guide the development and verification of future numerical models for tsunami inundation with debris transportation that can be potentially used to simulate r a wider range of realistic conditions.

7. Conclusion

This paper presents an experimental study of tsunami-driven debris advection over the flat testbed. We utilize two types of debris elements, which have the same shape but different materials (wood, HDPE) to create debris of different densities. We considered variations in the grouping of debris (wood only, mixed wood and HDPE, and HDPE only), parameterized by the mean specific gravity (SG_g), ranging from 0.65 (wood only) to 0.99 (HDPE only). We also considered the variation in starting conditions (e.g., mixed debris with wood debris on the seaward side or landward side; uniform, checker, random starting patterns). We introduced fixed obstacles landward of the initial debris field. *In-situ* instrumentation was used to quantify the flow hydrodynamics (free surface, velocity), and cameras suspended from above were used to quantify the debris trajectories. Tests were conducted with the same forcing condition (water level and wavemaker displacement time history) and the same bathymetric conditions throughout the tests. In total, 46 tests were conducted. The main contributions and conclusions of this study are summarized below:

1. The less-dense debris group ($SG_g = 0.65$, wood) moved further and had less spread compared to a more dense debris group ($SG_g = 0.99$, HDPE).
2. The mean longitudinal displacement $\overline{D_x^*}$ of less dense debris decreased linearly as the amount of more dense debris increased (Fig. 11) in the debris group due to the interrupting influence by the more dense debris during the advection. However, the mean longitudinal displacement $\overline{D_x^*}$ of the more dense debris was uniform. In summary, the more dense debris affected the mean longitudinal displacement of the less dense debris, but the converse was not true.
3. The spreading angle of less dense debris increase slightly ($+3^\circ$) as the number of higher density elements were added. The spreading angle of the more dense debris decreased (-9.7°) as the less dense elements were added.
4. For groups with mixed debris, the initial configuration (e.g., wood debris on the seaward side or landward side of the HDPE debris; uniform, checker, random starting patterns) had little effect on the mean longitudinal displacement $\overline{D_x^*}$ or spreading angle.
5. The cases with less dense debris (wood) only had a 30% higher probability of collision with the obstacles compared to the cases with the more dense (HDPE) debris only. When the debris types were mixed, the less dense debris has a lower probability of collision with the obstacles.
6. Overall, the reflected wave and interaction among different debris play a role in the probability of collision. However, the density of each debris element was a dominant factor in determining the collision probability.
7. The leading-edge flow velocity is spatially uniform ($\overline{u}$=1.4 m/s) and greater than the less dense debris ($\overline{u}$=1 m/s) or more dense debris ($\overline{u}$=0.7 m/s). The flow velocity of both debris types varied spatially and was sensitive to the flow depth, a draft of debris, and the existence of obstacles.

In general, this paper highlights the importance of considering debris density in estimating the longitudinal distance and spreading angle. These variables were less dependent on the initial configuration of the debris field. Future studies should consider other aspects of the phenomena, including a better understanding of the potential impact by debris on obstacles, the role of the return flow in determining the debris trajectory, and investigations of the obstacles that more realistically reflect urban shorelines subjected to strong overland flow.

CRediT authorship contribution statement

Hyoungsu Park: Conceptualization, Formal analysis, Investigation, Writing – original draft, Writing – review & editing, Investigation, Data curation, Visualization. **Myung-Jin Koh:** Formal analysis, Writing – original draft, Data curation. **Daniel T. Cox:** Conceptualization, Investigation, Writing – review & editing, Supervision, Funding acquisition. **Mohammad Shafiqual Alam:** Investigation, Writing – review & editing. **Sungwon Shin:** Conceptualization, Writing – review & editing.

Declaration of competing interest

The authors declare that they have no known competing financial interests or personal relationships that could have appeared to influence the work reported in this paper.

Acknowledgment

The authors gratefully acknowledge the help of Sean Duncan, Adam Kean, Joaquin Moris Barra, Pedro Lomonaco, and Tim Maddux to set up and performed this experiment. The authors thank the two anonymous reviewers whose constructive comments significantly improved this manuscript. This material in this study is based upon work partially supported by the National Science Foundation under awards 1519679 and 1661315. Any opinions, findings, and conclusions or recommendations expressed in this material are those of the author and do not necessarily reflect the views of the National Science Foundation.

References

Aghl, P.P., Naito, C.J., Riggs, H.R., 2015. Estimation of demands resulting from inelastic axial impact of steel debris. Eng. Struct. 82, 11–21.
American Society of Civil Engineers, 2016. Minimum Design Loads and Associated Criteria for Buildings and Other Structures. ASCE/SEI 7-16.
ASCE, 2017. Minimum design loads and associated criteria for buildings and other structures. ASCE/SEI 7-16.
Bourgeois, J., MacInnes, B., 2010. Tsunami boulder transport and other dramatic effects of the 15 November 2006 central Kuril Islands tsunami on the island of Matua. Zeitschrift für Geomorphologie, Supplementary Issues 54 (3), 175–195.
Çelik, M., Ergun, Ö., Keskinocak, P., 2015. The post-disaster debris clearance problem under incomplete information. Oper. Res. 63 (1), 65–85.
Chock, G.Y., 2016. Design for tsunami loads and effects in the ASCE 7-16 standard. J. Struct. Eng. 142 (11), 04016093.
Chock, G., Robertson, I., Kriebel, D., Francis, M., Nistor, I., 2013. Tohoku, Japan, Earthquake and Tsunami of 2011: performance of structures under Tsunami loads. Am. Soc. Civ. Eng.
Duncan S, DT Cox, A Barbosa, P Lomonaco, H Park, MS Alam, C Yu, Physical modeling of progressive damage and failure of wood-frame coastal residential sructures due to waves and surge forces, Coast. Eng., (submitted, 7/2020)..
Etienne, S., Buckley, M., Paris, R., Nandasena, A.K., Clark, K., Strotz, L., Chagué-Goff, C., Goff, J., Richmond, B., 2011. The use of boulders for characterising past tsunamis: lessons from the 2004 Indian Ocean and 2009 South Pacific tsunamis. Earth Sci. Rev. 107 (1–2), 76–90.
FEMA, U., 2007. Public Assistance—Debris Management Guide. Dept. of Homeland Security, Washington, DC.
Fritz, H.M., Phillips, D.A., Okayasu, A., Shimozono, T., Liu, H., Mohammed, F., Skanavis, V., Synolakis, C.E., Takahashi, T., 2012. The 2011 Japan tsunami current velocity measurements from survivor videos at Kesennuma Bay using LiDAR. Geophys. Res. Lett. 39 (7).
Goseberg, N., 2013. Reduction of maximum tsunami run-up due to the interaction with beachfront development–application of single sinusoidal waves (2013). Nat. Hazards Earth Syst. Sci. 13. Nr. 11.
Goseberg, N., Stolle, J., Nistor, I., Shibayama, T., 2016. Experimental analysis of debris motion due the obstruction from fixed obstacles in tsunami-like flow conditions. Coast. Eng. 118, 35–49.
Imamura, F., Goto, K., Ohkubo, S., 2008. A numerical model for the transport of a boulder by tsunami. J. Geophys. Res.: Oceans 113 (C1).
Kihara, N., Kaida, H., 2020. Applicability of tracking simulations for probabilistic assessment of floating debris collision in tsunami inundation flow. Coast Eng. J. 62 (1), 69–84.
Ko, H.S., Cox, D.T., Riggs, H.R., Naito, C.J., 2015. Hydraulic experiments on impact forces from tsunami-driven debris. J. Waterw. Port, Coast. Ocean Eng. 141 (3), 04014043.
Lin, N., Vanmarcke, E., 2008. Windborne debris risk assessment. Probabilist. Eng. Mech. 23 (4), 523–530.
Martinez, E., Maamaatuaiahutapu, K., Taillandier, V., 2009. Floating marine debris surface drift: convergence and accumulation toward the South Pacific subtropical gyre. Mar. Pollut. Bull. 58 (9), 1347–1355.
Miller, J.A., Carlton, J.T., Chapman, J.W., Geller, J.B., Ruiz, G.M., 2018. Transoceanic dispersal of the mussel Mytilus galloprovincialis on Japanese tsunami marine debris: an approach for evaluating rafting of a coastal species at sea. Mar. Pollut. Bull. 132, 60–69.
Murray, C.C., Maximenko, N., Lippiatt, S., 2018. The influx of marine debris from the Great Japan Tsunami of 2011 to North American shorelines. Mar. Pollut. Bull. 132, 26–32.
Naito, C., Cercone, C., Riggs, H.R., Cox, D., 2014. Procedure for site assessment of the potential for tsunami debris impact. J. Waterw. Port, Coast. Ocean Eng. 140 (2), 223–232.
Nistor, I., Goseberg, N., Stolle, J., 2017a. Tsunami-driven debris motion and loads: a critical review. Front. Built Environ. 3, 2.
Nistor, I., Goseberg, N., Stolle, J., Mikami, T., Shibayama, T., Nakamura, R., Matsuba, S., 2017b. Experimental investigations of debris dynamics over a horizontal plane. J. Waterw. Port, Coast. Ocean Eng. 143 (3), 04016022.
Paris, R., Fournier, J., Poizot, E., Etienne, S., Morin, J., Lavigne, F., Wassmer, P., 2010. Boulder and fine sediment transport and deposition by the 2004 tsunami in Lhok Nga (western Banda Aceh, Sumatra, Indonesia): a coupled offshore–onshore model. Mar. Geol. 268 (1–4), 43–54.
Park, H., Cox, D.T., 2019. Effects of advection on predicting construction debris for vulnerability assessment under multi-hazard earthquake and tsunami. Coast. Eng. 153, 103541.
Park, H., Cox, D.T., Lynett, P.J., Wiebe, D.M., Shin, S., 2013. Tsunami inundation modeling in constructed environments: a physical and numerical comparison of free-surface elevation, velocity, and momentum flux. Coast. Eng. 79, 9–21.
Park, H., Cox, D.T., Barbosa, A.R., 2018. Probabilistic tsunami hazard assessment (PTHA) for resilience assessment of a coastal community. Nat. Hazards. https://doi.org/10.1007/s11069-018-3460-3.
Prasetya, G., Black, K., de Lange, W., Borrero, J., Healy, T., 2012. Debris dispersal modeling for the great Sumatra Tsunamis on Banda Aceh and surrounding waters. Nat. Hazards 60 (3), 1167–1188.
Qin, X., Motley, M.R., Marafi, N.A., 2018. Three-dimensional modeling of tsunami forces on coastal communities. Coast. Eng. 140, 43–59.
Riggs, H.R., Cox, D.T., Naito, C.J., Kobayashi, M.H., Piran Aghl, P., Ko, H.S., Khowitar, E., 2014. Experimental and analytical study of water-driven debris impact forces on structures. J. Offshore Mech. Arctic Eng. 136 (4).
Rueben, M., Cox, D., Holman, R., Shin, S., Stanley, J., 2015. Optical measurements of tsunami inundation and debris movement in a large-scale wave basin. J. Waterw. Port, Coast. Ocean Eng. 141 (1), 04014029.
Shafiei, S., Melville, B.W., Shamseldin, A.Y., Beskhyroun, S., Adams, K.N., 2016. Measurements of tsunami-borne debris impact on structures using an embedded accelerometer. J. Hydraul. Res. 54 (4), 435–449.
Shekhar, K., Winter, A.O., Alam, M.S., Arduino, P., Miller, G.R., Motley, M.R., Eberhard, M.O., Barbosa, A.R., Lomonaco, P., Cox, D.T., 2020. Conceptual evaluation of tsunami debris field damming and impact forces. J. Waterw. Port, Coast. Ocean Eng. 146 (6), 04020033.
Stolle, J., Nistor, I., Goseberg, N., Mikami, T., Shibayama, T., 2017. Entrainment and transport dynamics of shipping containers in extreme hydrodynamic conditions. Coast Eng. J. 59, 1750011, 03.
Stolle, J., Takabatake, T., Nistor, I., Mikami, T., Nishizaki, S., Hamano, G., Ishii, H., Shibayama, T., Goseberg, N., Petriu, E., 2018a. Experimental investigation of debris damming loads under transient supercritical flow conditions. Coast. Eng. 139, 16–31.
Stolle, J., Goseberg, N., Nistor, I., Petriu, E., 2018b. Probabilistic investigation and risk assessment of debris transport in extreme hydrodynamic conditions. J. Waterw. Port, Coast. Ocean Eng. 144 (1), 04017039.
Stolle, J., Nistor, I., Goseberg, N., Petriu, E., 2020. Development of a probabilistic framework for debris transport and hazard assessment in tsunami-like flow conditions. J. Waterw. Port, Coast. Ocean Eng. 146 (5), 04020026.
Sugawara, D., Goto, K., Jaffe, B.E., 2014. Numerical models of tsunami sediment transport—current understanding and future directions. Mar. Geol. 352, 295–320.
Tachikawa, M., 1983. Trajectories of flat plates in uniform flow with application to wind-generated missiles. J. Wind Eng. Ind. Aerod. 14 (1–3), 443–453.
Tomiczek, T., Prasetyo, A., Mori, N., Yasuda, T., Kennedy, A., 2016. Physical modelling of tsunami onshore propagation, peak pressures, and shielding effects in an urban building array. Coast. Eng. 117, 97–112.
Tomiczek, T., Wargula, A., Lomónaco, P., Goodwin, S., Cox, D., Kennedy, A., Lynett, P., 2020. Physical model investigation of mid-scale mangrove effects on flow hydrodynamics and pressures and loads in the built environment. Coast. Eng. 162, 103791.
von Häfen, H., Stolle, J., Nistor, I., Goseberg, N., 2021. Side-by-side entrainment and displacement of cuboids due to a tsunami-like wave. Coast. Eng. 164, 103819.
Winter, A.O., Alam, M.S., Shekhar, K., Motley, M.R., Eberhard, M.O., Barbosa, A.R., et al., 2020. Tsunami-like wave forces on an elevated coastal structure: effects of flow shielding and channeling. J. Waterw. Port, Coast. Ocean Eng. 146 (4), 04020021.
Xia, J., Falconer, R.A., Xiao, X., Wang, Y., 2014. Criterion of vehicle stability in floodwaters based on theoretical and experimental studies. Nat. Hazards 70 (2), 1619–1630.
Yao, Y., Huang, Z., Lo, E.Y., Shen, H.T., 2014. A preliminary laboratory study of motion of floating debris generated by solitary waves running up a beach. J. Earthq. Tsunami 8, 1440006, 03.
Yeh, H., Barbosa, A., Mason, B.H., 2014. Tsunamis effects in man-made environment. In: Encyclopedia of complexity and systems science, pp. 1–27.